

Propagation of pop ups in kirigami shells

Ahmad Rafsanjani^{a,b,1}, Lishuai Jin^{a,c,1}, Bolei Deng^a, and Katia Bertoldi^{a,d,e,2}

^aJohn A. Paulson School of Engineering and Applied Sciences, Harvard University, Cambridge, MA 02138; ^bDepartment of Materials, ETH Zürich, 8093 Zürich, Switzerland; ^cDepartment of Mechanics, Tianjin University, Tianjin 300072, China; ^dKavli Institute, Harvard University, Cambridge, MA 02138; and ^eWyss Institute for Biologically Inspired Engineering, Harvard University, Cambridge, MA 02138

Edited by John A. Rogers, Northwestern University, Evanston, IL, and approved March 12, 2019 (received for review October 15, 2018)

Kirigami-inspired metamaterials are attracting increasing interest because of their ability to achieve extremely large strains and shape changes via out-of-plane buckling. While in flat kirigami sheets, the ligaments buckle simultaneously as Euler columns, leading to a continuous phase transition; here, we demonstrate that kirigami shells can also support discontinuous phase transitions. Specifically, we show via a combination of experiments, numerical simulations, and theoretical analysis that, in cylindrical kirigami shells, the snapping-induced curvature inversion of the initially bent ligaments results in a pop-up process that first localizes near an imperfection and then, as the deformation is increased, progressively spreads through the structure. Notably, we find that the width of the transition zone as well as the stress at which propagation of the instability is triggered can be controlled by carefully selecting the geometry of the cuts and the curvature of the shell. Our study significantly expands the ability of existing kirigami metamaterials and opens avenues for the design of the next generation of responsive surfaces as demonstrated by the design of a smart skin that significantly enhances the crawling efficiency of a simple linear actuator.

kirigami | buckling | propagative instability | metamaterials | phase transition

Kirigami—the Japanese art of cutting paper—has recently inspired the design of highly stretchable (1–8) and morphable (9–17) mechanical metamaterials that can be easily realized by embedding an array of cuts into a thin sheet. An attractive feature of these systems is that they are manufactured flat and then, exploit elastic instabilities to transform into complex 3D configurations (2–6, 13). Remarkably, the morphology of such buckling-induced 3D patterns can be tuned by varying the arrangement and geometry of the cuts (2–4) as well as the loading direction (13). However, in all kirigami systems proposed to date, the buckling-induced pop-up process occurs concurrently through the entire system, resulting in a simultaneous shape transformation.

The coexistence of two phases has been observed at both the microscopic and macroscopic scales in a variety of systems, including phase-transforming materials (18–22), dielectric elastomers (23, 24), and thin-walled elastic tubes (25, 26) (Movie S1). While these systems are very different in nature from each other, they all share a nonconvex free energy function that, for specific conditions, has two minima of equal height. When such a situation is reached, the homogeneous deformation becomes unstable, and a mixture of two states emerges. The new phase initially nucleates near a local imperfection and then, under prevailing conditions, propagates through the entire system (21, 24–26).

Here, we demonstrate via a combination of experiments and numerical/theoretical analyses that kirigami structures can also support the coexistence of two phases, the buckled one and the unbuckled one. Specifically, we show that, in thin cylindrical kirigami shells subjected to tensile loading, the buckling-induced pop-up process initially localizes near an imperfection and then, as the deformation is increased, progressively spreads through the cylinder at constant stress. We find that the curvature of the cylinder is the essential ingredient to observe this phenomenon, as it completely changes the deformation mechanism of the

hinges. In kirigami sheets, the initially flat hinges buckle out of plane, leading to a monotonic stress–strain relationship for the unit cell. By contrast, in kirigami shells, the initially bent ligaments snap to their second stable configuration, resulting in a nonmonotonic stress–strain curve typical of phase-transforming materials (18–22).

Experiments

We start by testing under uniaxial tension a kirigami flat sheet and a corresponding cylindrical shell. Both structures are fabricated by laser cutting triangular cuts arranged on a triangular lattice with lattice constants $l = 12$ mm and $\gamma = \pi/3$ separated by hinges with width $\delta = l/16$ (resulting in a rectangular unit cell with width $L = 2l \cos \pi/6$ and height $H = 2l \sin \pi/6$) into polyester plastic sheets (Artus Corporation) of thickness $t = 76.2 \mu\text{m}$ with Young's modulus $E = 4.33$ GPa and Poisson's ratio $\nu = 0.4$ (Fig. 1A). The flat kirigami sheet comprises an array of 2×20 cuts, while the cylindrical shell has 8×20 cuts and is created by bending an initially flat perforated sheet into a cylinder with radius $r \sim nL/(2\pi)$ (n denotes the number of unit cells along the circumference of the cylinder) (Fig. 1B) and gluing the two overlapping edges with a thin adhesive layer (SI Appendix, section 1 and Movie S2 have fabrication details).

In Fig. 1C and D, we show snapshots of the kirigami sheet and kirigami shell at different levels of applied deformation. We find that the responses of the two structures are remarkably different (Movie S3). In the kirigami sheet at a critical strain, all triangular features simultaneously pop up, forming a uniform 3D

Significance

Kirigami—the Japanese art of cutting paper—has become an emergent tool to realize highly stretchable devices and morphable structures. While kirigami structures are fabricated by simply perforating an array of cuts into a thin sheet, the applied deformation and associated instabilities can be exploited to transform them into complex 3D morphologies. However, to date, such reconfiguration always happen simultaneously through the system. By borrowing ideas from phase-transforming materials, we combine cuts and curvature to realize kirigami structures in which deformation-induced shape reconfiguration initially nucleates near an imperfection and then, under specific conditions, spreads through the system. We envision that such control of the shape transformation could be used to design the next generation of responsive surfaces and smart skins.

Author contributions: A.R., L.J., and K.B. designed research; A.R., L.J., and B.D. performed research; A.R., L.J., and B.D. analyzed data; B.D. developed the theoretical model; and A.R., L.J., B.D., and K.B. wrote the paper.

The authors declare no conflict of interest.

This article is a PNAS Direct Submission.

Published under the PNAS license.

¹A.R. and L.J. contributed equally to this work.

²To whom correspondence should be addressed. Email: bertoldi@seas.harvard.edu.

This article contains supporting information online at www.pnas.org/lookup/suppl/doi:10.1073/pnas.1817763116/-DCSupplemental.

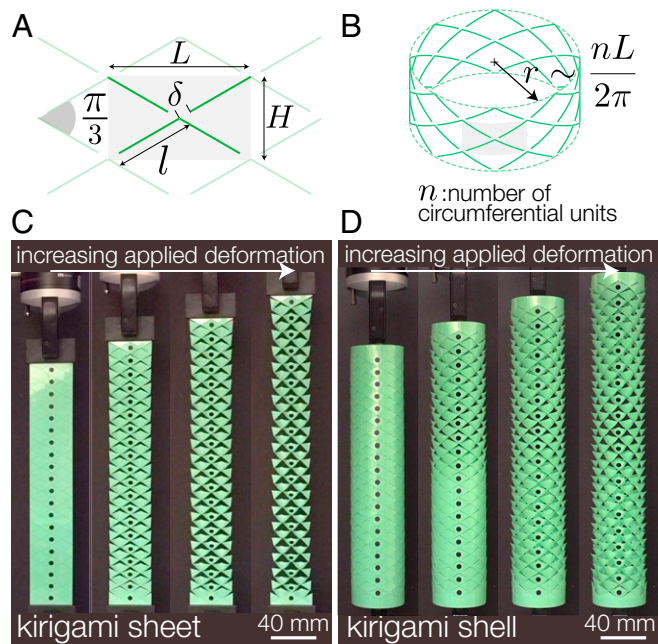


Fig. 1. (A) Schematic of a kirigami structure that comprises an array of triangular cuts. The unit cell has width L and height H , and it is highlighted in gray. (B) Schematic of a kirigami cylindrical shell comprising $n = 8$ unit cells along the circumference. (C) Experimental images of a kirigami sheet with a triangular pattern characterized by $\delta/l = 0.0625$ (with $l = 12$ mm) at different levels of deformation. The pop-up process occurs concurrently through the entire system. (D) Experimental images of a kirigami sheet fabricated by rolling a sheet with a triangular pattern characterized by $\delta/l = 0.0625$ (with $l = 12$ mm and $n = 8$ unit cells along the circumference) at different levels of deformation. The pop-up process initiates at the top end of the sample and then, spreads toward the bottom one as $\bar{\epsilon}$ is increased. The thickness of all kirigami structures is $t = 76.2$ μm .

textured surface that becomes more accentuated for increasing deformation (Fig. 1C). By contrast, in the cylindrical kirigami shell, the pop-up process initiates at the top end of the sample and then, spreads toward the other end as the applied deformation is increased (Fig. 1D). Note that the pop-up process in our shells typically starts at one of the ends of the shell, since these act as imperfection. As a matter of fact, a local reduction in the size of the hinges has to be introduced to cause the propagation to start from a different location (*SI Appendix, Fig. S7 and Movie S9*).

Next, to better characterize the response of our structures, during the tests, we monitor black circular markers located at the base of the triangular cuts (Fig. 1C and D) and use their position to determine both the applied strain, $\bar{\epsilon}$, and the local strain in longitudinal direction for the i th row of cuts, ϵ_i , as

$$\bar{\epsilon} = \frac{z_q - z_p}{Z_q - Z_p} - 1, \quad \epsilon_i = \frac{z_{i+1} - z_i}{Z_{i+1} - Z_i} - 1, \quad [1]$$

where z_i and Z_i denote the positions of the i th marker in the deformed and undeformed configurations, respectively. We choose $p = 3$ and $q = 18$ to minimize boundary effects. Moreover, we use a custom laser profilometer and track the deformation of a horizontal line passing through the hinges at different levels of applied deformation.

In Fig. 2A and B, we report the evolution of the local strain ϵ_i as a function of $\bar{\epsilon}$ for the kirigami sheet and shell, respectively. In full agreement with our previous observations, we find that, in the kirigami sheet, the local strain increases uniformly through the structure and is always very close to the applied deformation

(i.e., $\epsilon_i \sim \bar{\epsilon} \forall i$) (Fig. 2A). Differently, the contour map for the kirigami cylindrical shell shows a nonvertical boundary between popped/open (yellow in Fig. 2B) and unpopped/closed (blue in Fig. 2B) regions (Fig. 2B)—a clear signature of sequential opening. Furthermore, the constant slope of such boundary indicates that the pop-up process propagates at constant rate of applied deformation (*SI Appendix, section 2*).

To gain more insight into the physics behind the different behavior observed in the kirigami sheet and kirigami shell, we then investigate the deformation mechanism of their hinges. By inspecting their 3D-scanned profiles (Fig. 2C and D), we find that they deform in a very different way. In the kirigami sheet, the hinges are initially flat and act as straight beams (5, 13); for a critical level of applied deformation, they buckle and subsequently bend out of plane. By contrast, in the kirigami shell, the initially bent hinges behave as bistable arches (27) and snap to their second stable configurations, which are characterized by curvature inversion. This observation is fully consistent with the results of Figs. 1 and 2, since snapping is always accompanied by a highly nonlinear stress–strain response, which is typical of phase-transforming materials (18–22). As a matter of fact, while elastic structures comprising arrays of beams that buckle under the applied load have been shown to display homogeneous

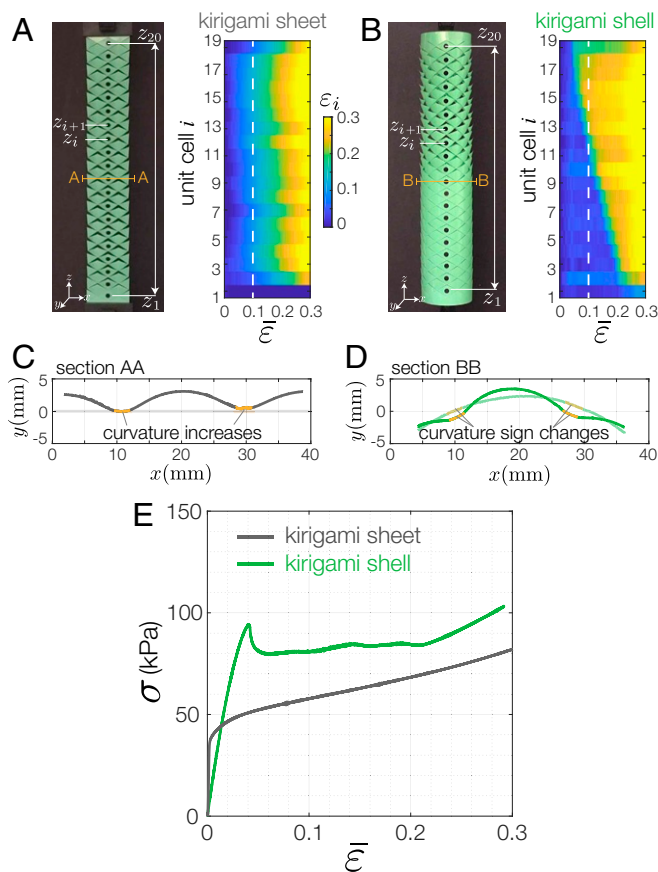


Fig. 2. (A and B) Evolution of the local strain ϵ_i as a function of $\bar{\epsilon}$ for the (A) kirigami sheet shown in Fig. 1C and (B) the kirigami shell shown in Fig. 1D. (C and D) Projection in the xy plane of a line passing through hinges (such lines are indicated in orange in A and B) as reconstructed using a custom laser profilometer for (C) the kirigami sheet and (D) the kirigami shell. The deformation of the hinges is highlighted in orange. (E) Experimental stress–strain curves for the kirigami sheet and the kirigami shell considered in Fig. 1. Note that the amplitude of the peak observed for the kirigami shell is correlated to the size of imperfection that triggers the pop up (*SI Appendix, Fig. S20*).

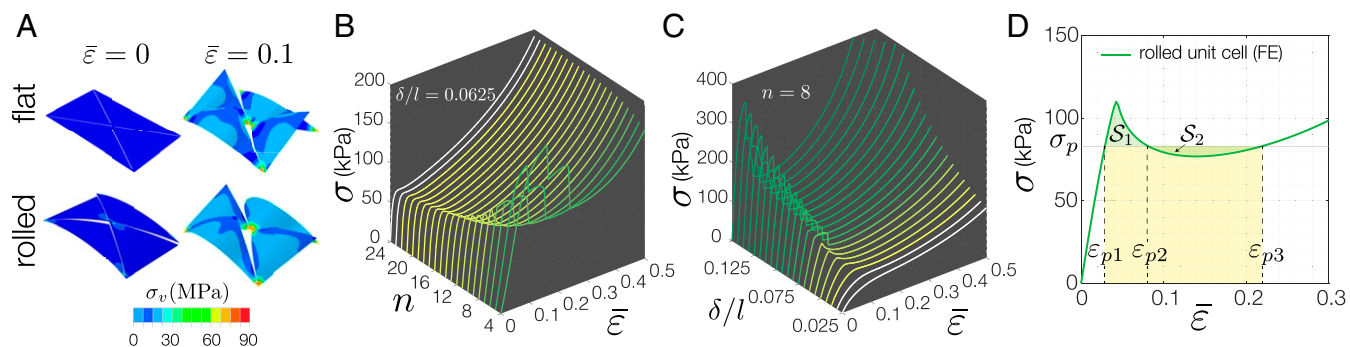


Fig. 3. (A) FE snapshots of flat and rolled unit cells (characterized by $\delta/l = 0.0625$ with $l = 12$ mm) at $\bar{\varepsilon} = 0$ and 0.1 . (B) Strain–stress curves of unit cells with $\delta/l = 0.0625$ as a function of n . (C) Strain–stress curves of unit cells with $n = 8$ as a function of δ/l . (D) Stress–strain response of unit cells with $\delta/l = 0.0625$ and $n = 8$. In the plot, we highlight the energy barrier S_1 , the steady-state propagation stress σ_p , and the critical strains ε_{p1} , ε_{p2} , and ε_{p3} . The thickness of all kirigami unit cells is $t = 76.2$ μm .

pattern transformations (13, 28), sequential events are typically observed in systems based on snapping units (29–31).

Finally, in Fig. 2E, we compare the stress–strain curves of the kirigami sheet and the kirigami shell. We find that the response of the kirigami sheet is typical of buckling-based structures (32) and that it is characterized by an initial linear regime (during which all hinges bend in plane) followed by a plateau stress (caused by the homogeneous buckling-induced pop-up process). The cylindrical kirigami shell also exhibits these two regimes, but the transition between them is more abrupt and characterized by a sharp load drop. At the peak, a small portion of the kirigami shell near the top end pops up, causing the unloading of the rest of the structure and a drop in stress. Subsequently, when the ligaments of the buckled region start to be stretched and become resistant to additional deformation, the pop-up process spreads sequentially through the entire structure, and the stress reaches a steady-state value $\sigma_p = 83.5$ kPa. Finally, after all units are fully popped up at $\bar{\varepsilon} \sim 0.22$, the stress starts to rise again because of additional stretching of all hinges.

Modeling

Having understood how the imposed curvature affects the deformation mechanism as well as the response of our kirigami structures, we now use a combination of numerical and analytical tools to quantify this effect. To begin with, we conduct nonlinear finite element (FE) within Abaqus/Standard to investigate the effect of both the ligament width δ and the curvature $1/r$ (which is proportional to $1/n$) on the response of unit cells subjected to uniaxial tension (SI Appendix, section 4). We find that, for $\delta/l \in [0.025, 0.15]$ and $n \in [4, 24]$, the applied deformation always triggers a buckling instability that induces the pop up of the triangular features (Fig. 3A and Movie S7). However, the stress–strain response is found to be significantly affected by both δ and n (Fig. 3B and C). For large values of n (i.e., for small curvatures), all unit cells are characterized by monotonic stress–strain curves (Fig. 3B) irrespective of δ/l . Differently, below a critical n , the stress–strain response becomes nonmonotonic characterized by a peak, a subsequent drop in load, and final stiffening. Furthermore, we find that, by either decreasing n (at constant δ/l) (Fig. 3B) or increasing δ/l (at constant n) (Fig. 3C), the peak becomes more accentuated and is eventually followed by a sharp drop.

At this point, we want to emphasize that the nonmonotonic up–down–up behavior observed for most of our rolled unit cells is typical of elastic structures supporting propagative instabilities (25, 26). Remarkably, it has been shown that the Maxwell construction (33) can be applied to such stress–strain curves to determine several key parameters that characterize the behavior of our curved kirigami shell (25, 26). Specifically,

by equating the area of the two lobes formed by the $\sigma(\varepsilon)$ curve (i.e., by imposing $S_1 = S_2$) (Fig. 3D), we can identify (i) the propagation stress σ_p , (ii) the energy barrier S_1 , and (iii) the critical strains ε_{p1} , ε_{p2} , and ε_{p3} (Fig. 3D). For $\bar{\varepsilon} < \varepsilon_{p1}$, the structure deforms homogeneously, and all triangular features are unpopped, whereas for $\varepsilon_{p1} < \bar{\varepsilon} < \varepsilon_{p3}$, the pop-up process initiated at the top end of the sample spreads toward the other end.

While Maxwell construction enables us to easily determine several parameters, it does not provide any information on the width and the shape of the transition zone. This motivates the derivation of a more detailed model based on a 1D array of

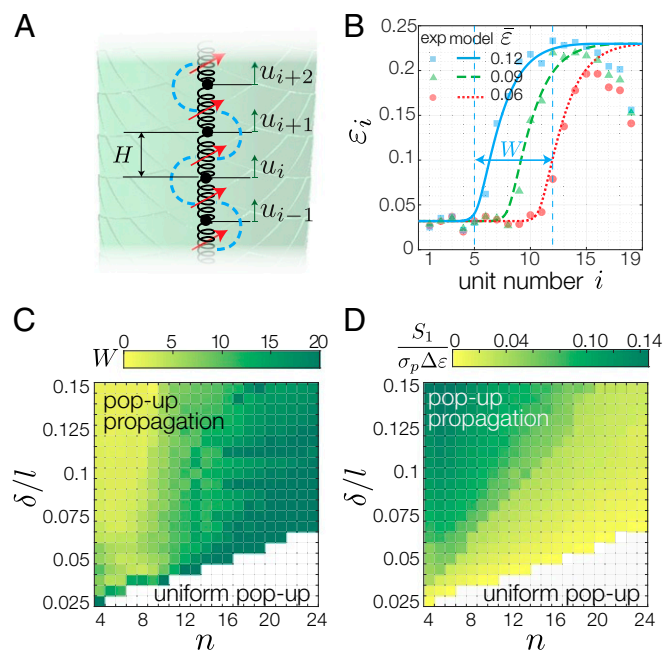


Fig. 4. (A) Schematic of our model comprising a 1D array of nonlinear springs. The blue dashed lines indicate the strain gradient interactions that we account for. (B) Comparison between the strain distribution predicted by our model and measured in experiments for the cylindrical kirigami shell shown in Fig. 1B. (C) Phase diagram of the width W of the transition zone as predicted by our model. (D) Phase diagram of the energy barrier of the kirigami shells with triangular cut pattern. S_1 (shaded green area in Fig. 3D) was normalized by the total energy required for phase transition [i.e., $\sigma_p(\varepsilon_{p3} - \varepsilon_{p1})$] obtained from 441 unit cell FE simulations. The thickness of all kirigami structures is $t = 76.2$ μm .

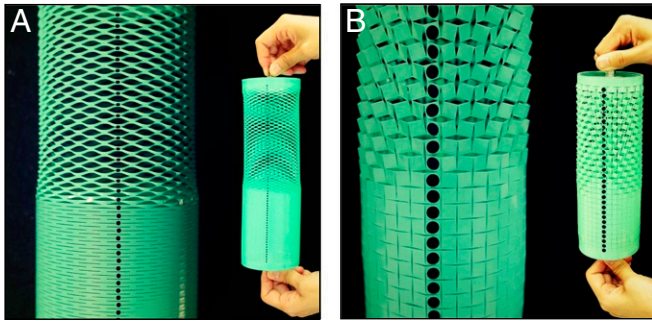


Fig. 5. (A) Experimental images of a kirigami cylindrical shell with $n = 20$ and linear cuts characterized by $\delta/l = 0.2$ (with $l = 12$ mm) at $\bar{\varepsilon} \approx 0.2$. (B) Experimental images of a kirigami cylindrical shell with $n = 20$ and orthogonal cuts characterized by $\delta/l = 0.08$ (with $l = 6$ mm) at $\bar{\varepsilon} \approx 0.1$. The thickness of kirigami shells is $t = 76.2 \mu\text{m}$.

N nonlinear springs (Fig. 4A) in which the response of the i th element is described as

$$F_i(u_i, u_{i+1}) = nLt \times \sigma(\varepsilon_i) = nLt \times \sigma\left(\frac{u_{i+1} - u_i}{H}\right), \quad [2]$$

where $\sigma(\varepsilon_i)$ is the nonlinear stress–strain response of the unit cell and $u_i = z_i - Z_i$ (Fig. 4A). We then write the strain energy of the system when subjected to a constant force $F_p = \sigma_p nLt$ as

$$\begin{aligned} \Pi = & U - F_p(u_{N+1} - u_1) \\ = & \sum_{i=1}^N nLt \int_0^{u_{i+1} - u_i} \sigma\left(\frac{u_{i+1} - u_i}{H}\right) d(u_{i+1} - u_i) \\ & - F_p(u_{N+1} - u_1) + \sum_{i=2}^N \frac{1}{2} nLtG(u_{i+1} - 2u_i + u_{i-1})^2, \end{aligned} \quad [3]$$

where the last term (and the coefficient G) is introduced to capture the effect of the strain gradient (34–36), which significantly affects the response of our kirigami structures given the strong coupling between their unit cells (SI Appendix, section 4). It follows that the equilibrium equations are given by

$$\sigma(\varepsilon_i) - \sigma(\varepsilon_{i-1}) - G(\varepsilon_{i+1} - 3\varepsilon_i + 3\varepsilon_{i-1} - \varepsilon_{i-2}) = 0, \quad [4]$$

for $i = 3, \dots, N - 1$

where ε_i is defined in Eq. 1.

Next, we take the continuum limit of Eq. 4, retain the nonlinear terms up to the third order, and integrate it with respect to Z to obtain

$$GH^2 \frac{d^2 \varepsilon}{dZ^2} = \sigma(\varepsilon) - \sigma_p, \quad [5]$$

where Z denotes the initial coordinate along the longitudinal direction and $\varepsilon(Z)$ is a continuous function of Z . We have assumed that, at $Z \rightarrow -\infty$, the unit cells are unpopped and subjected to a strain ε_{p1} . Eq. 5 is the continuum-governing equation for our kirigami structures, and given a stress–strain curve of the unit cell $\sigma(\varepsilon)$, it can be numerically solved to obtain the strain distribution $\varepsilon(Z)$ within the structure as a function of the applied strain. To test the relevance of our model, in Fig. 4B, we focus on the cylindrical kirigami shell of Fig. 1B and compare the evolution of the strain along its axes as predicted by our model and measured in experiments at $\bar{\varepsilon} = 0.06, 0.09$, and 0.12 . Note that the model predictions are obtained by numerically integrating Eq. 5 with $\sigma(\varepsilon)$ predicted by an FE simulation conducted on the unit cell, σ_p equal to the Maxwell stress and $G = 428$ kPa

(SI Appendix, section 4). Moreover, since the solution of Eq. 5 is translational invariant with respect to Z , the position of the propagation front Z_0 at a given applied strain $\bar{\varepsilon}$ can be determined from the compatibility condition

$$\bar{\varepsilon} = \frac{1}{Z_q - Z_p} \int_{Z_p}^{Z_q} \varepsilon(Z) dZ, \quad [6]$$

where $p = 3$ and $q = 18$ (Eq. 1). We find that our model accurately captures the shape, width, and amplitude of the transition zone as well as its position as a function of the applied strain, confirming the validity of our approach.

Effect of Geometry

While in Fig. 4B, we focus on a specific geometry, it is important to point out that our model can be used to efficiently characterize the propagation front as a function of the curvature of the shell, the hinge size, and the arrangement of the cuts. In Fig. 4C, we focus on kirigami structures with triangular cuts and report the evolution of the normalized width of the propagation front, W [which is defined as the width of region in which the strain changes by $0.9(\varepsilon_{p3} - \varepsilon_{p1})$] (Fig. 4B), as a function of δ/l and n . First, the results of our model indicate that, as the curvature of the kirigami shell increases (i.e., for larger n), W monotonically increases so that propagation of instability becomes less and less visible. In the limit of flat sheets, all unit cells are characterized by monotonic stress–strain curves, and only homogeneous pop up is possible (white region in Fig. 4C). Second, we find that, by increasing δ/l , at constant n , the propagation of instabilities becomes

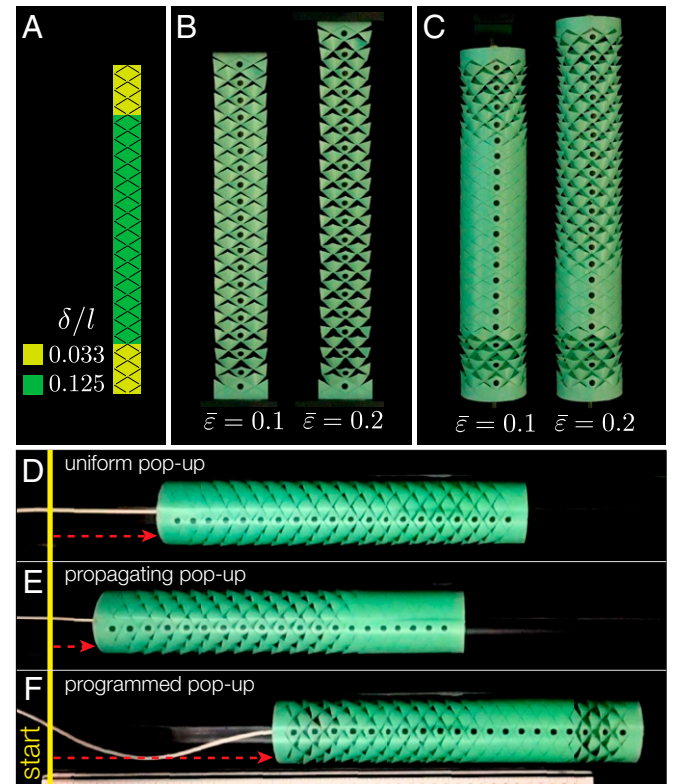


Fig. 6. (A) Schematic of our patterned kirigami surface. (B and C) Experimental images of the heterogeneous (B) kirigami sheet and (C) kirigami shell at $\bar{\varepsilon} = 0.1$ and 0.2 . (D–F) Snapshots of our kirigami-skinned crawlers with triangular cuts characterized by (D) $\delta/l = 0.033$ (uniform pop up), (E) $\delta/l = 0.125$ (propagating pop up), and (F) $\delta/l = 0.125$ for the central units and $\delta/l = 0.033$ for first three units at two ends (programmed pop up).

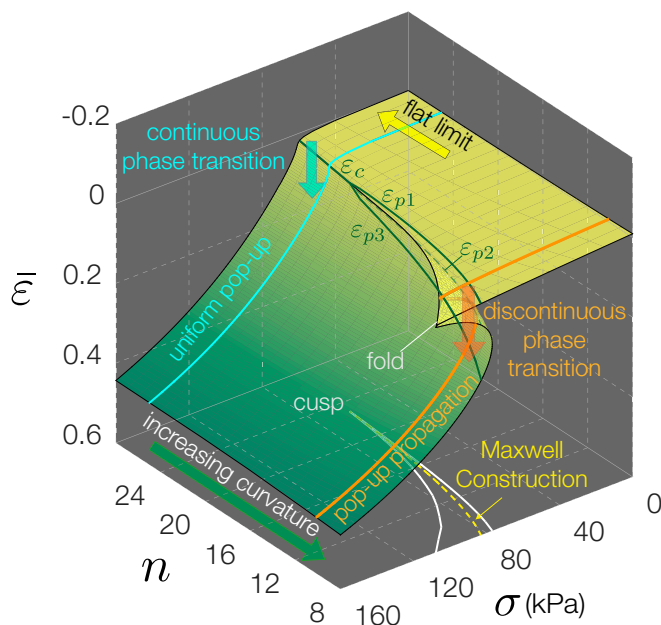


Fig. 7. Behavior surface for cylindrical kirigami shells with triangular cuts characterized by $l = 12$ mm, $\delta/l = 0.0625$, and $t = 76.2$ μm . The continuous sequence of states of equilibrium experienced by the shell on loading corresponds to a curve on the behavior surface. The behavior surface is smooth, but its projection on $n - \sigma$ contains two folds and a cusp. For shells with small curvature (i.e., for large n), the path does not reach the folds (blue line), and uniform pop ups occur at a critical strain ε_c associated with out-of-plane buckling of hinges. By increasing the curvature of the shell, the path eventually intersects the folds (red line). Inside the cusp, popped and unpopped regions coexist, and pop ups can propagate with a deformation path that passes from a stable unpopped strain ε_{p1} to another stable popped strain ε_{p3} through an unstable intermediate strain ε_{p2} . The projection of the ε_{p1} (or ε_{p2} or ε_{p3}) curves on the $\sigma - n$ plane represents the loci of propagation stress given by Maxwell construction.

more accentuated as the width W of the transition zone monotonically decreases (Fig. 4C). It is also interesting to note that the width of the transition zone is inversely proportional to the energy barrier S_1 (Fig. 4D). The largest values of S_1 are observed for unit cells with very large δ/l and very small n . For such units, the peak in stress is followed by a sharp drop, and the mechanical response is characterized by a discrete sequence of drops during propagation (SI Appendix, Fig. S15D), each corresponding to the opening of one row of cuts (Movie S4).

Notably, using our model in combination with FE analysis conducted on the unit cells, phase diagrams similar to those shown in Fig. 4C and D can be constructed for any cut pattern (SI Appendix, Fig. S16). Such diagrams can then be used to identify regions in the parameter space where propagation of instability is triggered. As examples, in Fig. 5, we report snapshots of cylindrical kirigami shells with a staggered array of linear cuts (3–5) and an array of mutually orthogonal cuts (1, 13). Both images clearly show the coexistence of the popped and unpopped phases (SI Appendix, Figs. S5 and S6 and Movies S5–S7) and further indicate that the characteristics of the phase transition can be controlled by carefully selecting the geometry of the cuts as well as the curvature of the shell. The kirigami shell with the linear pattern is characterized by a sharp propagation front spanning across about one unit cell and a propagation stress $\sigma_p = 177$ kPa (SI Appendix, Fig. S18), whereas the orthogonal cuts lead to a wider front spreading across about four unit cells and $\sigma_p = 320$ kPa (SI Appendix, Fig. S19).

Finally, we find that the coexistence of the buckled and unbuckled phases observed in our kirigami cylindrical shells

provides opportunities to realize surfaces with complex behavior that can be programmed to achieve a desired functionality. To demonstrate this, we consider a kirigami surface with 20 rows of triangular cuts separated by hinges with two different sizes. Specifically, we choose $\delta/l = 0.033$ for three rows near the two ends and $\delta/l = 0.125$ for the central rows (Fig. 6A). If such a surface is planar, no clear signature of the two different δ/l is apparent on stretching. Since the critical strains associated with the two considered δ/l are very close to each other ($\bar{\varepsilon}_c = 4.4275 \times 10^{-4}$ and 3.510×10^{-4} for $\delta/l = 0.033$ and 0.125 , respectively), all features pop up almost simultaneously and tilt fairly uniformly (Fig. 6B and SI Appendix, Fig. S9B). By contrast, if we use the heterogeneous kirigami sheet to form a cylinder with $n = 8$, on stretching, we find a clear sequence. First, the triangular features separated by ligaments with $\delta/l = 0.033$ pop up all together. Second, the pop ups propagate in the central region with $\delta/l = 0.125$ starting from the top (Fig. 6C, SI Appendix, Fig. S9C, and Movie S8). Remarkably, this sequencing achieved by simply patterning the sheet with regions characterized by different ligament widths can be exploited to design a smart skin that significantly enhances the crawling efficiency of a linear actuator (Fig. 6D–F). While all three kirigami-skinned crawlers advance on elongation and contraction of the actuator because of the anisotropic friction induced by the pop ups (7) (SI Appendix, section 3), the programmed pop up achieved in our patterned shell enhances the anchorage of the crawler to the substrate at two ends and significantly reduces the backslide (SI Appendix, Fig. S11B). As a result, the patterned crawler (Fig. 6F), which benefits from coexistence of popped and unpopped regions at desired locations, proceeds about twice as fast as the crawlers with a homogeneous array of triangular cuts with either $\delta/l = 0.033$ (Fig. 6D) or $\delta/l = 0.125$ (Fig. 6E).

Discussion and Conclusions

To summarize, we have shown that, in cylindrical kirigami shells, the buckled and unbuckled phases can coexist, with the pop-up process initially starting near an end and then, propagating along the cylinder at constant stress. In contrast to flat kirigami sheets, which can only support continuous phase transitions, by introducing curvature, the buckling-induced transformation exhibits discontinuity in the first derivative of the free energy, resulting in the coexistence of two phases (37). This remarkable difference in behavior arises, because the curvature transforms the ligaments from straight columns that buckle to bistable arches that snap. It should be also noted that such response is completely different from that of porous cylindrical shells, which under compression, exhibit uniform buckling-induced shape transformation (38–40), whereas it shares similarities with structures consisting of an array of beams resting on flexible supports, which have recently been shown to exhibit a very rich response (41, 42). The behavior of our system can be further understood by looking at its behavior surface (Fig. 7 shows a triangular pattern with $\delta/l = 0.125$). We find that, by increasing the curvature of the shell (i.e., by decreasing n), a cusp catastrophe emerges (43–45). The increase in curvature causes a progressively larger divergence between the top and bottom faces of the fold, making the discontinuous phase transition more pronounced. As such, the behavior surface in Fig. 7 further confirms that the curvature is the essential ingredient to trigger propagation of pop ups. However, we also find that the stresses introduced to bend the sheets into cylinders play an important role, as they increase the energy barrier and make the propagation more pronounced (SI Appendix, Fig. S14). Finally, we have shown that the characteristics of discontinuous phase transition can be tuned by carefully selecting the geometry of the kirigami structure. With such control on the phase transition in kirigami structures, we envision that these mechanical metamaterials could be used to design the

next generation of responsive surfaces as shown by the design of a smart skin that enhances the crawling efficiency of a linear actuator.

Materials and Methods

Details of fabrication of kirigami shells are described in *SI Appendix, section 1*. The protocol for experiments and additional experimental data for kirigami shells with triangular, linear, and orthogonal cut patterns are provided in *SI Appendix, section 2*. Principles of kirigami-skinned crawlers are presented in *SI Appendix, section 3*. Details of FE simulations and theoretical models are presented in *SI Appendix, section 4*.

1. Cho Y, et al. (2014) Engineering the shape and structure of materials by fractal cut. *Proc Natl Acad Sci USA* 111:17390–17395.
2. Zhang Y, et al. (2015) A mechanically driven form of Kirigami as a route to 3D mesostructures in micro/nanomembranes. *Proc Natl Acad Sci USA* 112:11757–11764.
3. Shyu TC, et al. (2015) A kirigami approach to engineering elasticity in nanocomposites through patterned defects. *Nat Mat* 14:785–789.
4. Blees MK, et al. (2015) Graphene kirigami. *Nature* 524:204–207.
5. Isobe M, Okumura K (2016) Initial rigid response and softening transition of highly stretchable kirigami sheet materials. *Sci Rep* 6:24758.
6. Dias MA, et al. (2017) Kirigami actuators. *Soft Matter* 13:9087–9092.
7. Rafsanjani A, Zhang Y, Liu B, Rubinstein SM, Bertoldi K (2018) Kirigami skins make a simple soft actuator crawl. *Sci Robotics* 3:eaar7555.
8. Hwang D-G, Trent K, Bartlett MD (2018) Kirigami-inspired structures for smart adhesion. *ACS Appl Mater Inter* 10:6747–6754.
9. Sussman DM, et al. (2015) Algorithmic lattice kirigami: A route to pluripotent materials. *Proc Natl Acad Sci USA* 112:7449–7453.
10. Neville RM, Scarpa F, Pirrera A (2016) Shape morphing Kirigami mechanical metamaterials. *Sci Rep* 6:31067.
11. Konaković M, et al. (2016) Beyond developable: Computational design and fabrication with auxetic materials. *ACM Trans Graph* 35:89.
12. Castle T, Sussman DM, Tanis M, Kamiñ RD (2016) Additive lattice kirigami. *Sci Adv* 2:e1601258.
13. Rafsanjani A, Bertoldi K (2017) Buckling-induced kirigami. *Phys Rev Lett* 118:084301.
14. Zhao Y, et al. (2017) Carbon nanotubes kirigami mechanical metamaterials. *Phys Chem Phys* 19:11032.
15. Yang N, Silverberg JL (2018) Decoupling local mechanics from large-scale structure in modular metamaterials. *Proc Natl Acad Sci USA* 112:11757–11764.
16. Liu Z, et al. (2018) Nano-kirigami with giant optical chirality. *Sci Adv* 4:eaat4436.
17. Yang Y, Dias MA, Holmes DP (2018) Multistable kirigami for tunable architected materials. *Phys Rev Mater* 2:110601.
18. Ericksen JL (1975) Equilibrium of bars. *J Elast* 5:191–201.
19. James RD (1979) Co-existent phases in the one-dimensional static theory of elastic bars. *Arch Ration Mech Anal* 72:99–140.
20. Abeyaratne R, Knowles JK (1991) Kinetic relations and the propagation of phase boundaries in solids. *Arch Ration Mech Anal* 114:119–154.
21. Shaw JA, Kyriakides S (1997) On the nucleation and propagation of phase transformation fronts in a NiTi alloy. *Acta Mater* 45:683–700.
22. Feng P, Sun QP (2006) Experimental investigation on macroscopic domain formation and evolution in polycrystalline NiTi microtubing under mechanical force. *J Mech Phys Sol* 54:1568–1603.
23. Zhao X, Hong W, Suo Z (2007) Electromechanical hysteresis and coexistent states in dielectric elastomers. *Phys Rev B* 76:134113.
24. Zhou J, Hong W, Zhao X, Zhang Z, Suo Z (2008) Propagation of instability in dielectric elastomers. *Int J Sol Struct* 45:3739–3750.
25. Chater E, Hutchinson JW (1984) On the propagation of bulges and buckles. *J Appl Mech* 51:269–277.
26. Kyriakides S (1993) Propagating instabilities in structures. *Adv Appl Mech* 30:67–189.
27. Plaut RH (2015) Snap-through of arches and buckled beams under unilateral displacement control. *Int J Sol Struct* 63:109–113.
28. Kang SH, et al. (2014) Complex ordered patterns in mechanical instability induced geometrically frustrated triangular cellular structures. *Phys Rev Lett* 112:098701.
29. Shan S, et al. (2015) Multistable architected materials for trapping elastic strain energy. *Adv Mater* 27:4296–4301.
30. Rafsanjani A, Akbarzadeh A, Pasini D (2015) Snapping mechanical metamaterials under tension. *Adv Mater* 27:5931–5935.
31. Restrepo D, Mankame ND, Zavattieri PD (2016) Phase transforming cellular materials. *Extreme Mech Lett* 27:5931–5935.
32. Bertoldi K, Reis PM, Willshaw S, Mullin T (2010) Negative Poisson's ratio behavior induced by an elastic instability. *Adv Mater* 22:361–366.
33. Maxwell JC (1875) On the dynamical evidence of the molecular constitution of bodies. *Nature* 11:357–359.
34. Mindlin RD (1964) Micro-structure in linear elasticity. *Arch Ration Mech Anal* 16: 51–78.
35. Polyzos D, Fotiadis DI (2012) Derivation of Mindlin's first and second strain gradient elastic theory via simple lattice and continuum models. *Int J Sol Struct* 49:470–480.
36. Audoly B, Hutchinson JW (2016) Analysis of necking based on a one-dimensional model. *J Mech Phys Sol* 97:68–91.
37. Jaeger G (1998) The Ehrenfest classification of phase transitions: Introduction and evolution. *Arch Hist Exact Sci* 53:51–81.
38. Matsumoto EA, Kamiñ RD (2012) Patterns on a roll: A method of continuous feed nanoprinting. *Soft Matter* 8:11038–11041.
39. Lazarus A, Reis PM (2015) Soft Actuation of structured cylinders through auxetic behavior. *Adv Eng Mater* 17:815–820.
40. Javid F, et al. (2016) Mechanics of instability-induced pattern transformations in elastomeric porous cylinders. *J Mech Phys Sol* 96:1–17.
41. Xu S, et al. (2015) Assembly of micro/nanomaterials into complex, three-dimensional architectures by compressive buckling. *Science* 347:154–159.
42. Abdullah AM, Nan K, Rogers JA, Hsia KJ (2016) Mismatch strain programmed shape transformation of curved bilayer-flexible support assembly. *Extreme Mech Lett* 7: 34–41.
43. Zeeman EC (1976) Catastrophe theory. *Sci Am* 234:65–83.
44. Thompson JMT (1975) Experiments in catastrophe. *Nature* 254:392–395.
45. Lu T, Cheng S, Li T, Wang T, Suo Z (2016) Electromechanical catastrophe. *Int J Appl Mech* 8:1640005.

Supplementary Information for

Propagation of pop-ups in kirigami shells

Ahmad Rafsanjani, Lishuai Jin, Bolei Deng and Katia Bertoldi

Corresponding Author: Katia Bertoldi
John A. Paulson School of Engineering and Applied Sciences
Harvard University, Cambridge, MA 02138, USA
E-mail: bertoldi@seas.harvard.edu

This PDF file includes:

Supplementary text
Figs. S1 to S25
Captions for Movies S1 to S9
References for SI reference citations

Other supplementary materials for this manuscript include the following:

Movies S1 to S9

Supporting Information Text

1. Fabrication

All kirigami structures investigated in this study are fabricated by laser cutting an array of cuts into polyester plastic sheets (Artus Corporation, NJ) with thickness $t \sim 76.2 \mu\text{m}$, Young's modulus $E = 4.33 \text{ GPa}$ and Poisson's ratio $\nu = 0.4$. As shown in Fig. S1, the laser cutting process results in cuts with width $w_c \simeq 0.1 \text{ mm}$.

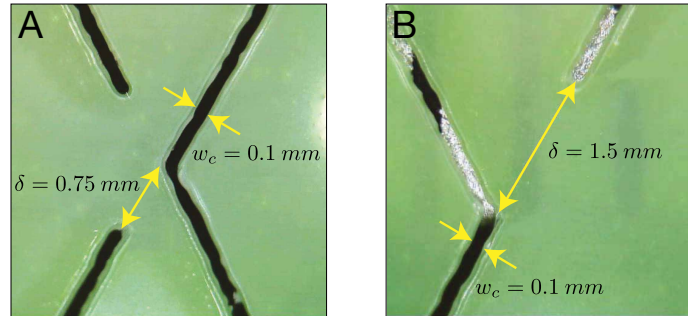


Fig. S1. Microscope image (Supereyes A005+ 5MP 500X) of a sheet laser cut to embed a triangular array of cuts with hinges of width (A) $\delta = 0.75 \text{ mm}$ and (B) $\delta = 1.50 \text{ mm}$. We find that the laser cutting process results in cuts with width $w_c \simeq 0.1 \text{ mm}$.

A. Kirigami shells. The cylindrical kirigami shells are then fabricated by rolling the laser cut kirigami sheets and attaching their two opposite edges to each other using a 0.07 mm thick double-sided adhesive sheet (23205-1009, Blick Art Materials, IL) (Figs. S2A and B). Note that a row of needles is used to ensure overlapping of the cuts located near the opposite edges and thus maintain the periodicity of the structure (Figs. S2C and D). Finally, two acrylic circular caps are glued to the both ends of the cylinder (Figs. S2E and F) and two screws are bolted at the center of the caps to facilitate attaching the samples to the tensile testing machine (see Supporting Movie S1).

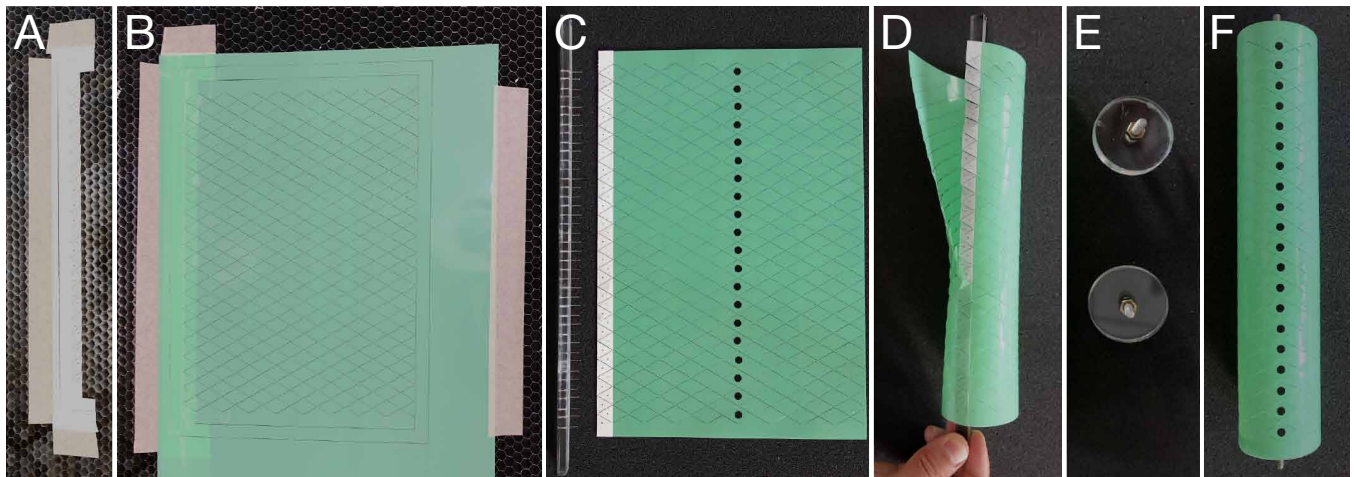


Fig. S2. Fabrication of a kirigami shell: (A) the double-sided adhesive is laser cut into the desired shape; (B) the polyester sheet is attached to the adhesive layer and the kirigami pattern is laser cut; (C) very thin adhesive black markers are attached to the sheet to track the deformation during testing; (D) the two edges of the sheet are attached together using needles to facilitate alignment; (E) two bolted acrylic caps are laser cut; (F) the caps are glued to the cylinder ends.

In this study three different kirigami patterns are considered:

- *Triangular pattern:* In this pattern, the cuts are arranged on a triangular lattice with lattice constants l and $\gamma = \pi/3$ (6). The unit cell considered in this study is highlighted in gray in Fig. S3A. It consists of a rectangular domain with width $L = 2l \cos \pi/6$ and height $H = 2l \sin \pi/6$ with embedded four cuts of length $l - \delta$ separated by hinges of width δ .
- *Linear pattern:* This pattern, which has been considered in several studies (2–4), comprises an array of staggered linear cuts of length $l - \delta$ separated in horizontal direction by hinges of width δ and in vertical direction by $l/8$. The unit cell considered in this study with width $L = l$ and height $H = l/4$ is highlighted in gray in Fig. S3B.
- *Orthogonal pattern:* This pattern consists of a square array of mutually orthogonal cuts (5). This perforation pattern introduces a network of square domains of edge l separated by hinges of width δ . The unit cell considered in this study with width $L = 2l$ and height $H = 2l$ is highlighted in gray in Fig. S3C.

Throughout the study, we fix the size of the unit cells (L and H) for each pattern. In particular, for the triangular pattern we choose $l = 12$ mm and $\gamma = \pi/3$, resulting in $L = 20.8$ mm and $H = 12$ mm, for the linear pattern $l = L = 12$ mm and $H = 3$ mm, and for the orthogonal pattern we choose $l = 6$ mm, leading to $L = H = 12$ mm. As a result, the number of units along the circumference n uniquely determine the size of cylinder. Specifically, the two acrylic caps that we glue at its two ends have radius $r = nL/(2\pi)$. However, it is important to note that, because of the cuts, the radius of the kirigami cylinder is not constant and varies both around the circumferential and axial directions.

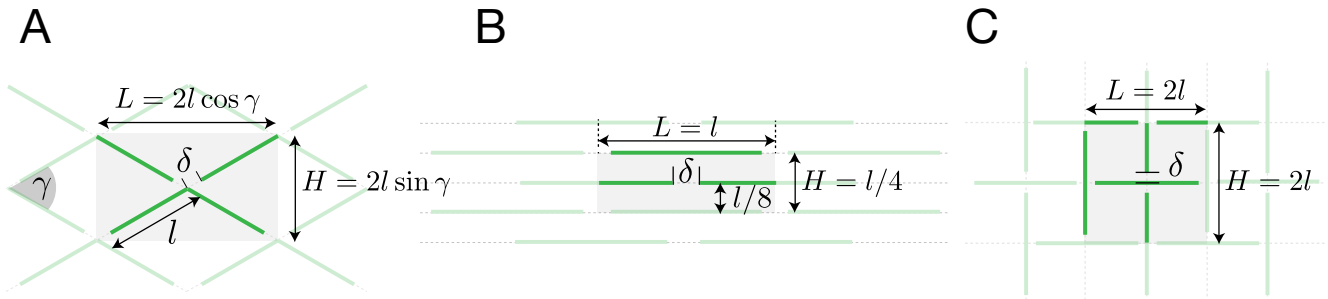


Fig. S3. Three different kirigami patterns are considered in this study: (A) triangular pattern with $\gamma = \pi/3$, (B) linear pattern and (C) orthogonal pattern. The unit cell of each pattern is shaded.

2. Experiments

The quasi-static uniaxial tensile response of the kirigami sheets and kirigami cylinders is probed using an uniaxial testing machine (Instron 5566) equipped with a 10N load cell. All tests are conducted under displacement control at a rate of 0.5 mm/s. During these tests we record the motion of the structures using a high-resolution camera (SONY RX100V) at a frame rate of 30 fps and extract their local deformation using an open-source digital image correlation and tracking package (7). We track the position of 20 markers uniformly placed on a vertical line (see Fig. S4A) and use these data to characterize both the applied deformation and the evolution of the local deformation as a function of the applied strain. Specifically, the applied strain $\bar{\varepsilon}$ is obtained as

$$\bar{\varepsilon} = \frac{z_q - z_p}{Z_q - Z_p} - 1, \quad [\text{S1}]$$

where z_i and Z_i denote the position of the i -th marker in the deformed and undeformed configuration, respectively. Note that, to minimize boundary effects, in Eq. S1 we choose $(p, q) = (3, 18)$, $(5, 55)$ and $(1, 30)$ for structures with triangular, linear and orthogonal patterns, respectively. As for the local deformation, focusing on the i -th row of cuts the normal strain in longitudinal direction is calculated as

$$\varepsilon_i = \frac{z_{i+1} - z_i}{Z_{i+1} - Z_i} - 1. \quad [\text{S2}]$$

Additional experimental results are provided in Figs. S4- S6.

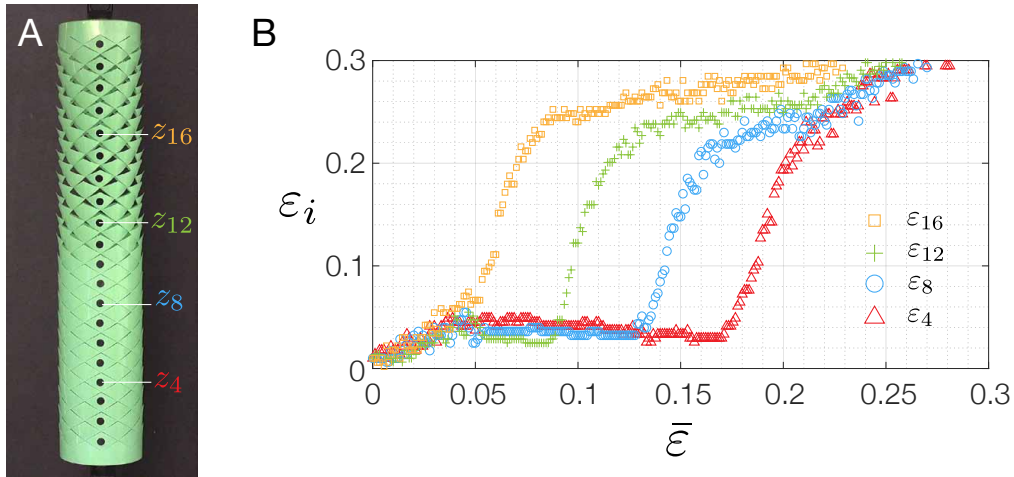


Fig. S4. Local strain distribution in a kirigami shell with triangular cuts: (A) Kirigami cylinder with $n = 8$ and $\delta/l = 0.0625$ (with $l = 12$ mm). (B) Evolution of ε_i (with $i = 4, 8, 12$ and 16) as a function of the the applied strain $\bar{\varepsilon}$.

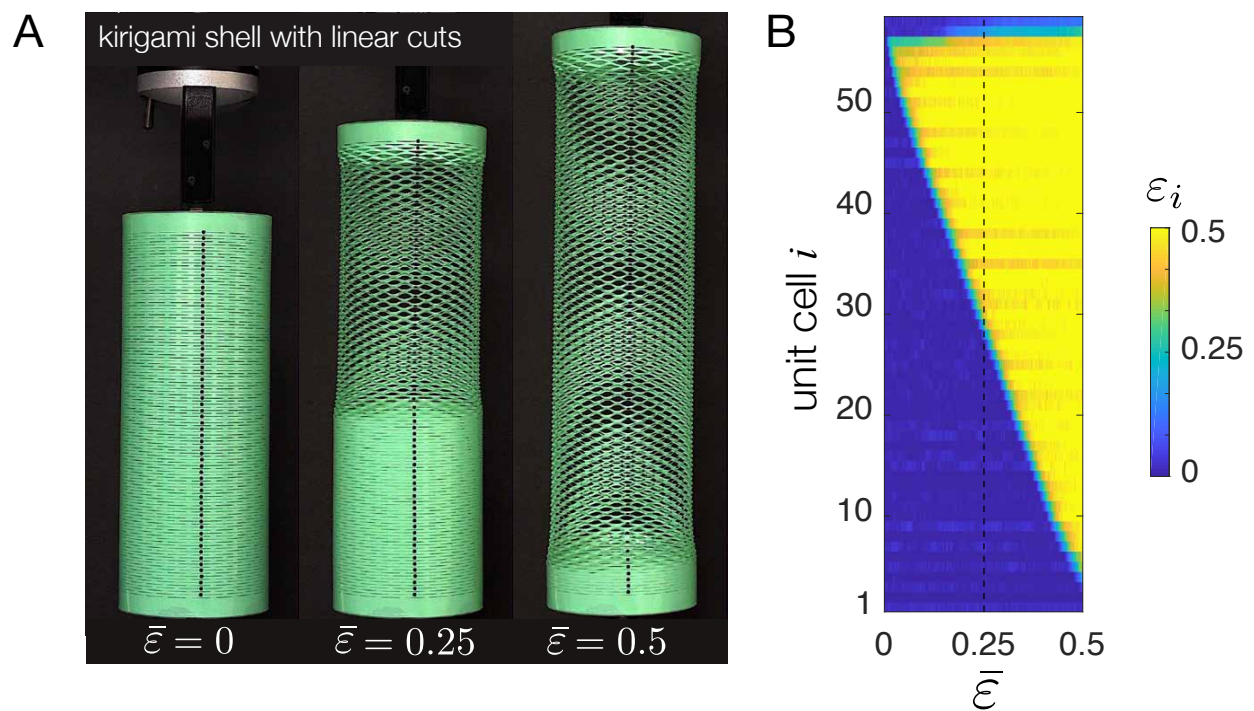


Fig. S5. (A) Snapshots of kirigami shells with linear cuts which are characterized by $\delta/l = 0.2$ (with $l = 12$ mm) and $n = 20$ at $\bar{\epsilon} = 0, 0.25$ and 0.5 . The snapshots clearly indicate that instability propagation in this kirigami shells is characterized by a very sharp and narrow front. (B) Contour map of local strains ϵ_i as a function applied strain $\bar{\epsilon}$ and unit cell number i .

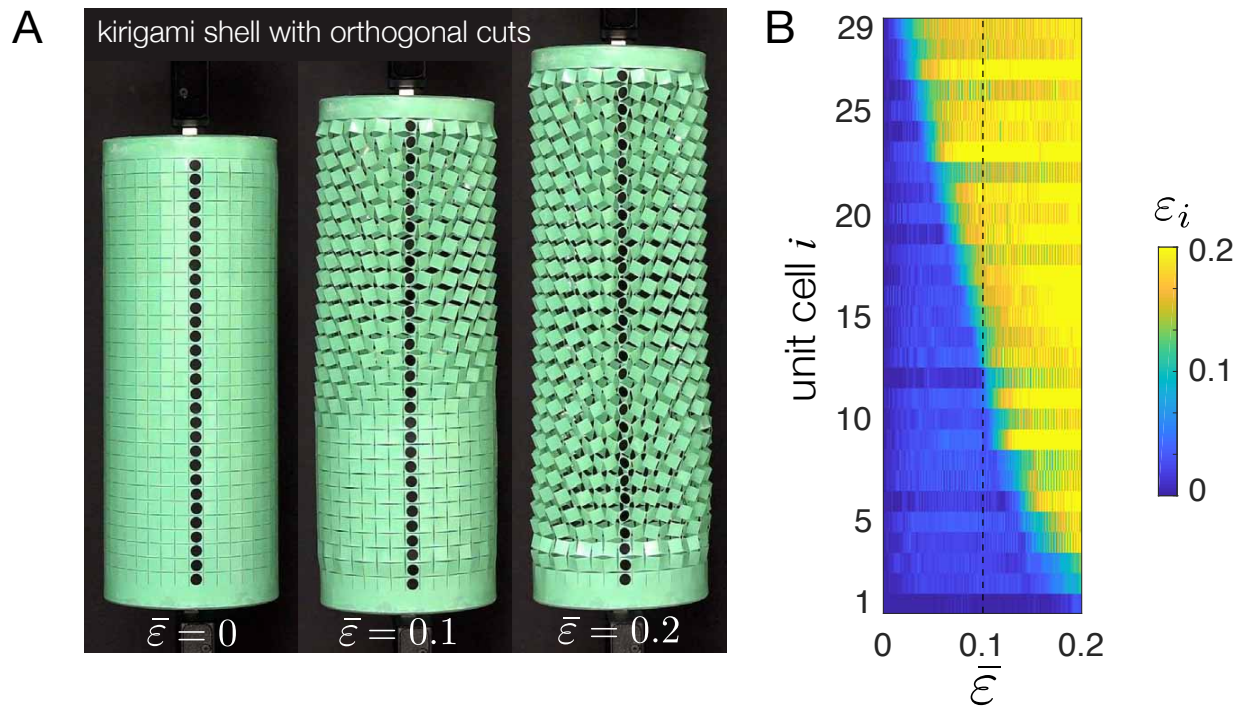


Fig. S6. (A) Snapshots of kirigami shells with orthogonal cuts which are characterized by $\delta/l = 0.08$ (with $l = 6$ mm) and $n = 20$ at $\bar{\epsilon} = 0, 0.1$ and 0.2 . The snapshots clearly indicate that instability propagation in this kirigami shells is characterized by a wider front compared to that found for the shell with linear pattern considered in Fig. S5. (B) Contour map of local strains ϵ_i as a function applied strain $\bar{\epsilon}$ and unit cell number i . The orthogonal pattern has a wider front compared to linear pattern.

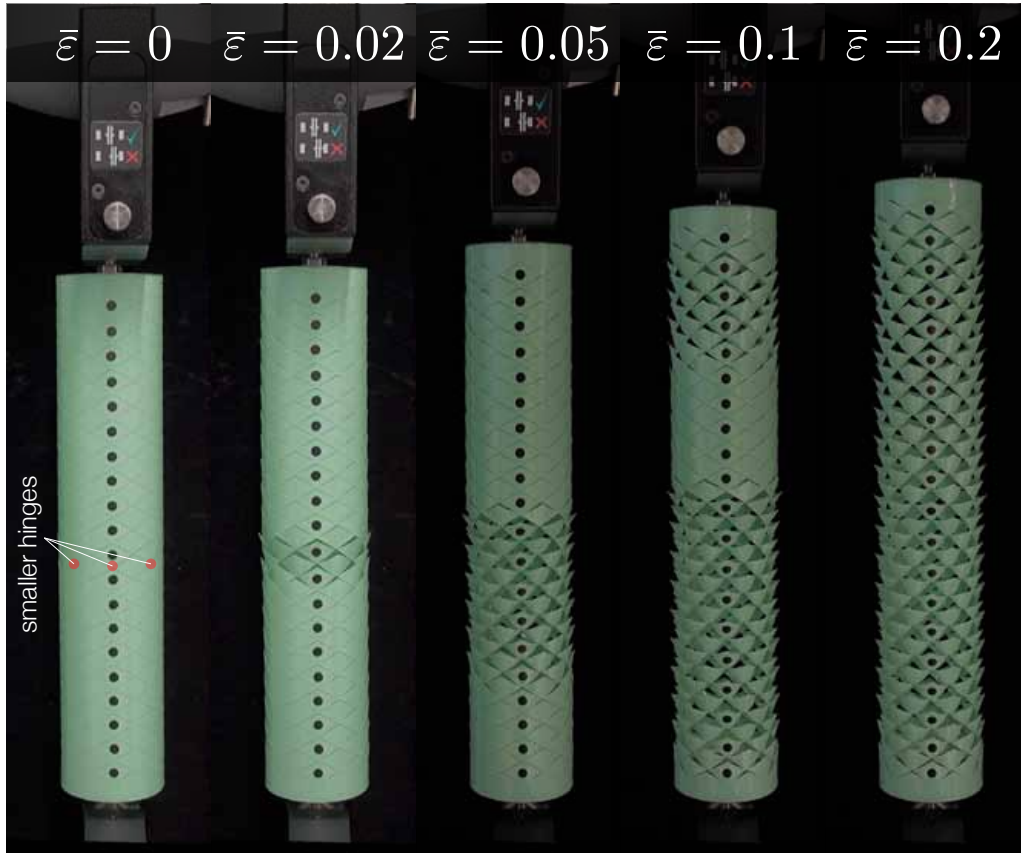
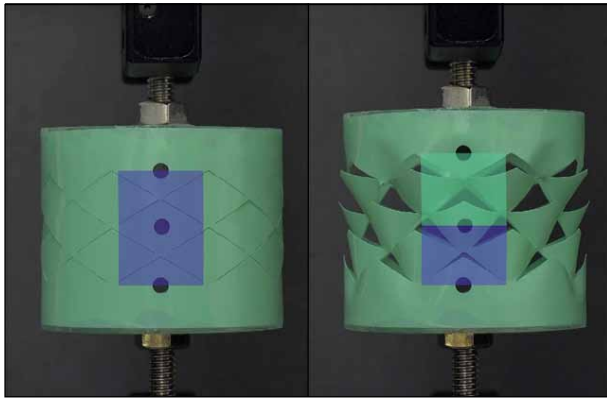


Fig. S7. Effect of imperfection. Snapshots of a kirigami shells with triangular cuts which is characterized by $\delta/l = 0.125$ (with $l = 12$ mm) and $n = 8$ at $\bar{\epsilon} = 0, 0.02, 0.05, 0.1$ and 0.2 . An imperfection is introduced in the middle of the shell by decreasing the width of one row of hinges (highlighted in red) to $\delta/l = 0.0625$. We find that the pop-ups initiate near the imperfection and propagate downwards until it reaches the bottom boundary. Further stretching triggers pop-ups from the top boundary and they continue propagating to reach the region which is already popped up. Finally the shell stretches uniformly (see Movie S9).

A



B

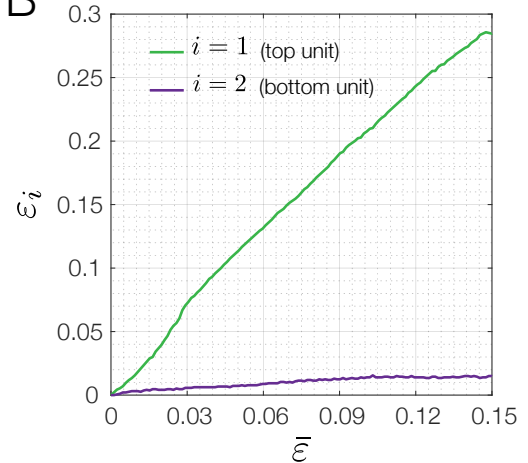


Fig. S8. Compliance of the boundaries. (A) In our experiments the pop-up process always starts from the top end (i.e. the end to which all triangular features are pointing), suggesting that the two ends of the kirigami shells introduce imperfections of different magnitude. To verify this, we test a kirigami shell with $n = 8$ and $\delta/l = 0.0625$ and monitor the local strain of the unit cells. (B) Evolution of ϵ_1 (i.e. the strain of the unit cell next to the top edge) and ϵ_2 (i.e. the strain of the unit cell next to the bottom edge) as a function of the applied deformation $\bar{\epsilon}$. We find that because of the asymmetry in geometry the unit cell next to the upper boundary is much more compliant - an observation that fully explains the initiation of the pop-ups from the top boundary.

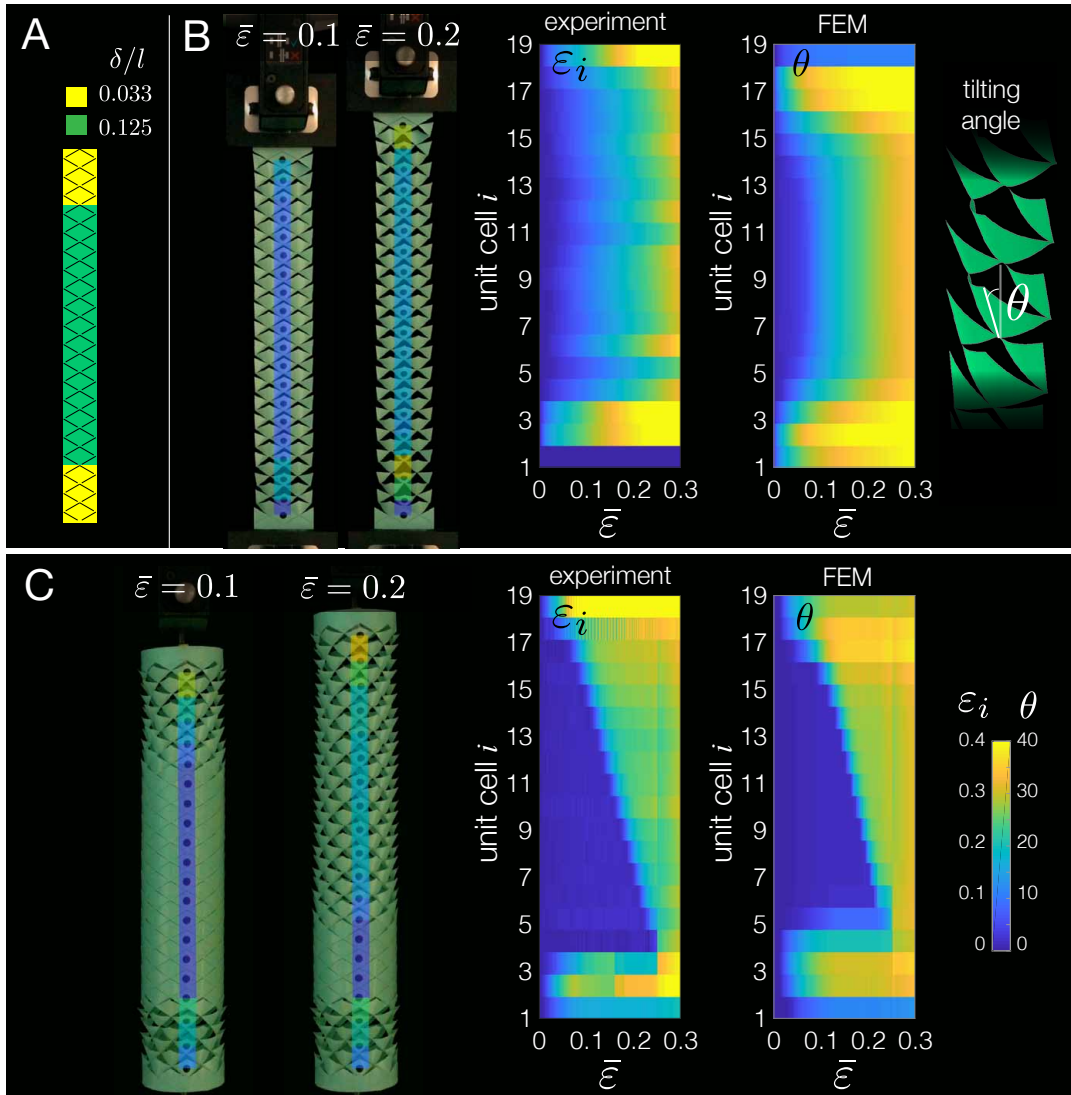


Fig. S9. (A) Schematic of our patterned kirigami surface. The triangular cuts are separated by ligaments with widths $\delta/l = 0.125$ in the central part (green region) and $\delta/l = 0.033$ near the two ends (yellow region). (B)-(C) Response of the patterned (B) kirigami sheet and (C) kirigami shell. The contour maps show the evolution of local strains ϵ_i and tilting angles θ_i as a function of the applied deformation. Note that the local strains ϵ_i are extracted from the experimental images, while θ_i are obtained from FE simulations conducted on super-cells.

3. Kirigami-skinned crawlers

In this study we also use the kirigami cylindrical shells as smart skins to enhance the crawling efficiency of a linear actuator. Specifically, the kirigami-skinned crawlers tested in this study comprise a 30 mL plastic syringe as linear actuator covered with a kirigami shell with triangular cuts (see Fig. S10A). The two ends of the plastic syringe are connected to two acrylic circular caps, that in turn are glued to the ends of the kirigami shell. A flexible tube passing through the rear cap then connects the actuator to a syringe pump which is programmed to cyclically inflate/deflate the plastic syringe. This results in an extension of the actuator of about 54 mm at 2.74 mm/s. Note that we choose a rigid linear actuator - as opposed to soft actuator used in our previous study (6) - to exclusively investigate the behavior of the kirigami skin. However, a fully soft crawler can be easily realized by simply replacing the plastic syringe with a soft actuator.

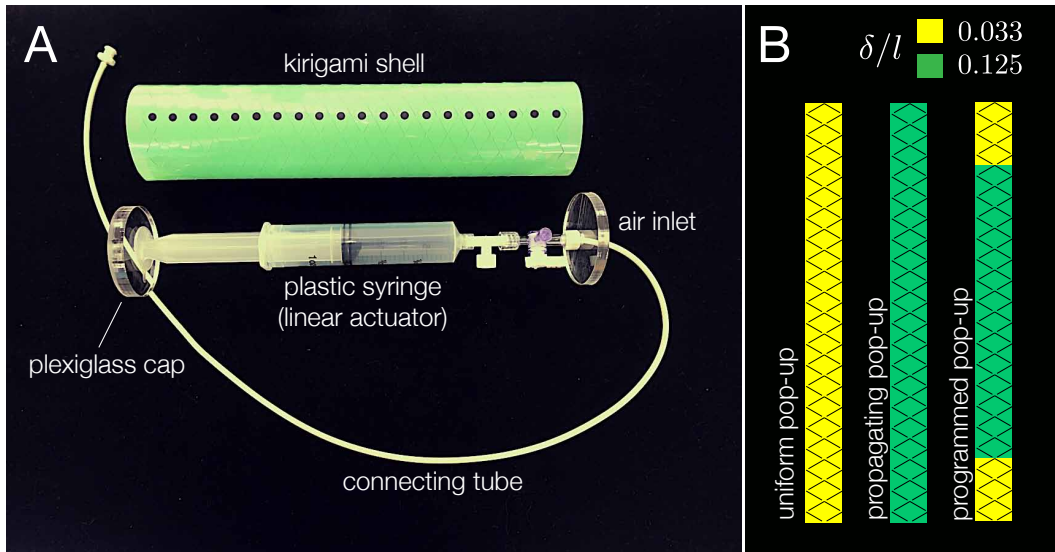


Fig. S10. (A) Components of the considered kirigami-skinned crawler. (B) Schematics of the three kirigami skins.

We consider three different kirigami skins, all comprising 8×20 triangular cuts with $l = 12$ mm and $\gamma = \pi/3$ (Fig. S10B):

- *Kirigami skin with uniform pop-up* with $\delta/l = 0.033$;
- *Kirigami skin with propagating pop-up* with $\delta/l = 0.125$;
- *Kirigami skin with programmed pop-up* with $\delta/l = 0.125$ for the central units and $\delta/l = 0.033$ for the first three units at the two ends.

To test the ability of the three crawlers to advance upon inflation and deflation of the syringe, we place them on the inner surface of an acrylic tube (with diameter of 65 mm) covered with a textile to increase friction. We find that for all three crawlers the elongation of the syringe triggers the pop-pop of the triangular scales, which in turn induces anisotropic frictional properties and enables our simple machines to move forward (6). However, since the anchorage to the ground is not perfect, there is always some backslide movement and not all the elongation induced by the syringe translates into advancement of the crawler (6). Remarkably, by comparing the performance of our three crawlers we find that the programmed pop-up achieved in our patterned shell enhances

the anchorage of the crawler to the substrate at two ends and significantly reduces the backslide (see Fig. S11B). As a result, the patterned crawler, which benefits from coexistence of popped and unpopped regions at desired locations, proceeds about twice faster than the other two.

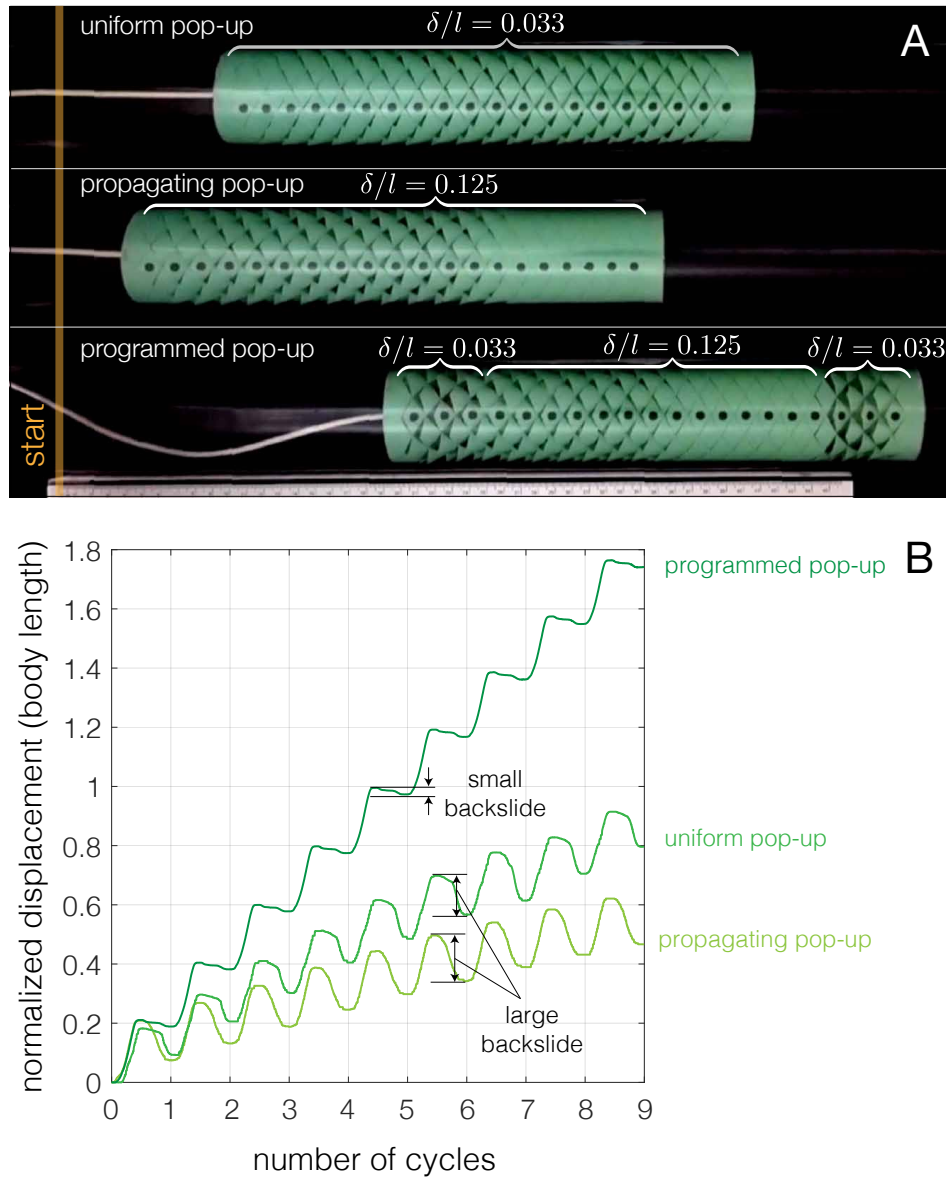


Fig. S11. (A) Snapshots of our kirigami-skinned crawlers with triangular cuts characterized by $\delta/l = 0.033$ (uniform pop-up), $\delta/l = 0.125$ and $\delta/l = 0.125$ for the central units and $\delta/l = 0.033$ for first three units at two ends (programmed pop-up). (B) Displacement of three crawlers normalized by their undeformed active body length (i.e. NH) as a function of the number of inflation/deflation cycles.

4. Modeling

To get a better understanding of the response of the considered kirigami structures, we investigate their behavior both numerically and analytically. First, we conduct Finite Element (FE) simulations on both unit cells and super-cells. Second, informed by these analyses, we establish an analytical model that predicts the stress required to trigger a propagative instability as well as the strain distribution within the structure during the propagation of the pop-ups.

A. Finite Element Simulations. To investigate the response of the kirigami structures under uniaxial stretch, we perform Finite Element (FE) Analyses using the commercial package ABAQUS 6.14/Standard (1). In all our analyses we discretize the sheets using four-node general-purpose shell elements with reduced integration and hourglass control (S4R element type) and, guided by our experiments (see Fig. S1) model the cuts as elongated rectangular voids with width of 0.1 mm. Since plasticity has little effect on the observed phenomena, the material behavior of the plastic sheets is captured using a linear elastic material model (with $E = 4.33$ GPa and $\nu = 0.4$). The response of the kirigami structures is then simulated conducting non-linear static simulations (*STATIC module in ABAQUS). Due to the existence of local buckling during the deformation, to facilitate convergence we also add volume-proportional damping to the model (using the option STABILIZE in ABAQUS) and set the dissipated energy fraction equal to $5e-4$ and the maximum ratio of stabilization to strain energy equal to 0.05. To reduce the computational cost and make sure the response of the system is not dominated by boundary effects, we conduct analysis on both unit cells and super-cells comprising $N \times 1$ unit cells. For the unit cells, we apply periodic boundary conditions to all four edges, whereas for the super-cells we apply periodic boundary conditions only to the left and right ones.

In the following we provide details on the simulations we conduct to investigate the response of (i) flat, (ii) rolled and (iii) curved kirigami sheets.

Flat kirigami sheets. The simulations conducted to investigate the response of flat kirigami sheets consist of two steps.

Step 1: we apply a small displacement (with amplitude $0.1t$) normal to the sheet either to the tip of the cuts (in case of the triangular patterns) or to the middle of the cuts (in case of the linear and orthogonal patterns). In this way we introduce a small imperfection into the mesh to guide the post-buckling analysis. Note that to facilitate convergence during this step no traction and displacement are applied to the nodes lying on the external edges of the models.

Step 2: We apply a strain ε to axially stretch the periodic cells. To simulate this on the unit cells, we apply periodic boundary conditions on all four edges. Specifically, we subject the unit cells to a macroscopic deformation

$$\bar{\mathbf{H}} = \varepsilon_{xx} \mathbf{e}_x \otimes \mathbf{e}_x + \varepsilon \mathbf{e}_z \otimes \mathbf{e}_z, \quad [\text{S3}]$$

by imposing the following periodic boundary conditions on all cell boundaries

$$\begin{aligned} u_\alpha^{A_i} - u_\alpha^{B_i} &= \bar{H}(X_\beta^{A_i} - X_\beta^{B_i}), \\ \theta_\alpha^{A_i} &= \theta_\alpha^{B_i} \quad i = 1, 2, \dots, N \end{aligned} \quad [\text{S4}]$$

where $u_\alpha^{A_i}$, $u_\alpha^{B_i}$, $\theta_\alpha^{A_i}$ and $\theta_\alpha^{B_i}$ ($\alpha = x, y$ and z) are the displacements and rotations of points periodically located on the boundary of the unit cell, $X_\beta^{A_i}$ and $X_\beta^{B_i}$ are their initial coordinates and N denotes the number of pairs of nodes periodically located on the boundary of the unit cell. Moreover, ε_{xx} is the stretch in transverse direction that is determined from $\sigma_{xx} = 0$. Note that the components of $\bar{\mathbf{H}}$ can be conveniently prescribed within the finite element framework using a set of virtual nodes.

The corresponding macroscopic first Piola-Kirchhoff stress $\bar{\mathbf{P}}$ is then obtained through virtual work considerations (11).

As for the super-cells, they are subjected to uniaxial tension by fixing all nodes on their top surfaces in x and y directions, while uniformly displacing them in z -direction. The applied nominal strain, ε , is then obtained as the ratio between the applied axial displacement and the initial length of the model. Moreover, the corresponding nominal stress, S , is calculated by dividing the total reaction force on the top edge by the undeformed cross-sectional area of the sample, $A = Lt$.

Rolled kirigami sheets. The simulations conducted to investigate the response of rolled kirigami sheets also consist of two steps. Note that the periodic boundary conditions derived below are validated by comparison with analytical expressions for the deformation of a homogeneous (i.e. without cuts) sheet.

Step 1: We transform the flat model to a cylindrical one. We start with a flat unit cell with length L and height H (see Fig. S12) and roll it into a sector of a cylinder. At this point it is important to note that, because of the cuts, the radius of the kirigami cylinder is not constant and varies both around circumference and along the axial direction. To determine the boundary conditions required to roll a flat periodic cell into a cylindrical one, we assume that the flat cell is located at a distance y_0 from the center of the cylinder and symmetrically positioned with respect to the y axis. Under these assumptions, we find that it can be rolled into a cylindrical shape when its *left* and the *right* edges are subjected to (see Fig. S12)

- a rotation with respect to the z -axis

$$\theta_z = \pm \frac{\pi}{n}, \quad [S5]$$

- displacements in circumferential and radial direction that satisfy

$$y_0^2 + \frac{L^2}{4} = (\rho \cos \delta\phi + u_\rho)^2, \quad \sin \delta\phi = \frac{u_\phi}{\rho} \quad [S6]$$

where ρ and ϕ are respectively the radial and angular coordinates of the nodes periodically located on the edges and $\delta\phi = \pi/n - \arctan L/(2y_0)$. Guided by Eqs. S5 and S6, we then apply the following

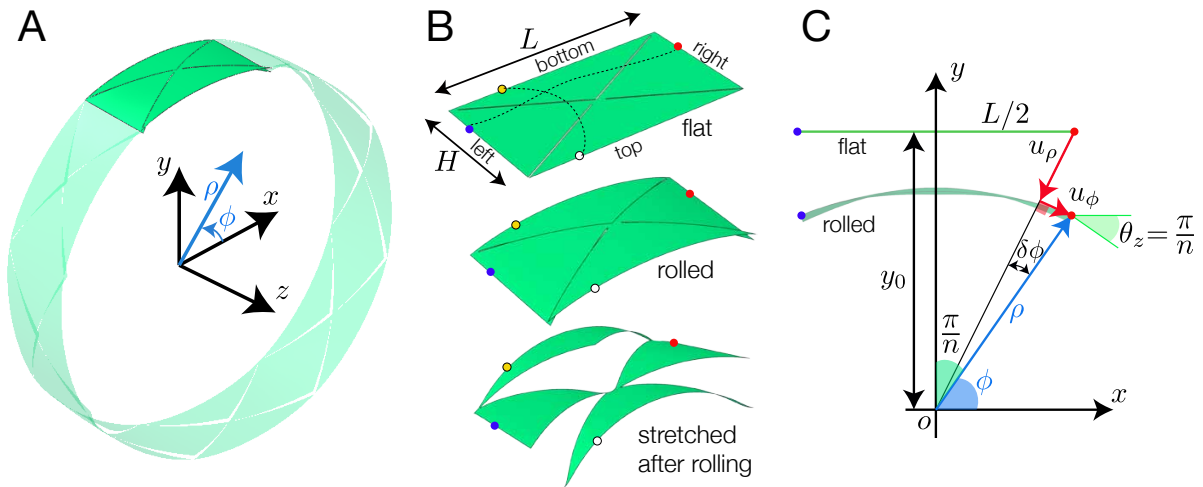


Fig. S12. (a) Schematic highlighting the coordinate system; (b) In our simulations, we start with a flat unit cell, we then roll it into a sector of a cylinder and finally stretch it. (c) Schematic highlighting the conditions that we use to roll the unit cell.

boundary conditions to the nodes periodically located on the left and right edges of the initially flat periodic cell

$$\begin{aligned}
u_\rho^{R_i} &= u_\rho^{L_i}, \\
u_\phi^{R_i} &= -\left(\sqrt{y_0^2 + L^2/4} - u_\rho^R\right) \tan \delta\phi, \\
u_\phi^{L_i} &= \left(\sqrt{y_0^2 + L^2/4} - u_\rho^L\right) \tan \delta\phi, \\
u_z^{R_i} &= u_z^{L_i}, \\
\theta_\rho^{L_i} &= -\theta_\rho^{R_i}, \\
\theta_\phi^{L_i} &= \theta_\phi^{R_i}, \\
\theta_z^{L_i} - \theta_z^{R_i} &= \frac{2\pi}{n}, \quad i = 1, 2, \dots, N
\end{aligned} \tag{S7}$$

where u_α^j and θ_α^j ($\alpha = \rho, \phi, z$ and $j = L_i, R_i$) are respectively the displacement and rotational degrees of freedom in the radial (ρ), circumferential (ϕ) and axial (z) directions of the i -th pair of nodes periodically located on the *right* (R) and *left* (L) edges of the unit cell.

As for the top and bottom edges, we let them to be free, so that, as observed when fabricating our kirigami cylinders, the periodic cell can axially contract as it is rolled. To achieve this on the unit cells, we use Eqs. S4 with

$$\bar{\mathbf{H}} = \varepsilon_{zz} \mathbf{e}_z \otimes \mathbf{e}_z \tag{S8}$$

and determine ε_{zz} by imposing $\sigma_{zz} = 0$.

Step 2: We apply a strain ε to axially stretch the periodic cells. To simulate this on the unit cells, we keep active the boundary conditions defined by Eqs. S7 on the left and right edges, while on the top and bottom edges we still use Eqs. S4, but with

$$\bar{\mathbf{H}} = \varepsilon \mathbf{e}_z \otimes \mathbf{e}_z. \tag{S9}$$

Finally, for super-cells with $n_z \times 1$ units, we impose Eq. S7 on their left and right edges, fix all the degrees of freedom of the nodes on the bottom edge (i.e. we set $u_z^B = u_\phi^B = u_\rho^B = \theta_\phi^B = \theta_\rho^B = \theta_z^B = 0$) and set $u_z^T = \varepsilon n_z H$ and $\theta_\rho^T = \theta_\phi^T = 0$, while leaving u_ρ^T, u_ϕ^T and θ_z^T free.

Validation of the periodic boundary conditions used to simulate the response of rolled kirigami sheets

To confirm the validity of the proposed approach to simulate the response of rolled cylinders, we compare FE results (obtained by using Eqs. S7 and Eqs. S4 with Eq. S8 and Eq. S9) against analytical solutions for a homogeneous sheet which is first rolled into a cylinder and then stretched (Fig. S13B). To derive such analytical solution, we start by noting that, when the bending radius r and the width of the sheet L are much larger than the sheet thickness t , during the rolling/bending process: (i) the cross section of the sheet remains planar; (ii) the neutral layer coincides with the mid-plane; (iii) there is no stress in radial direction (i.e. $\sigma_y = 0$); and (iv) there is no deformation in axial direction (i.e. $\varepsilon_z = 0$). Under these assumptions, the Hook's Law reads

$$\sigma_x = \frac{E\varepsilon_x}{1 - \nu^2}. \tag{S10}$$

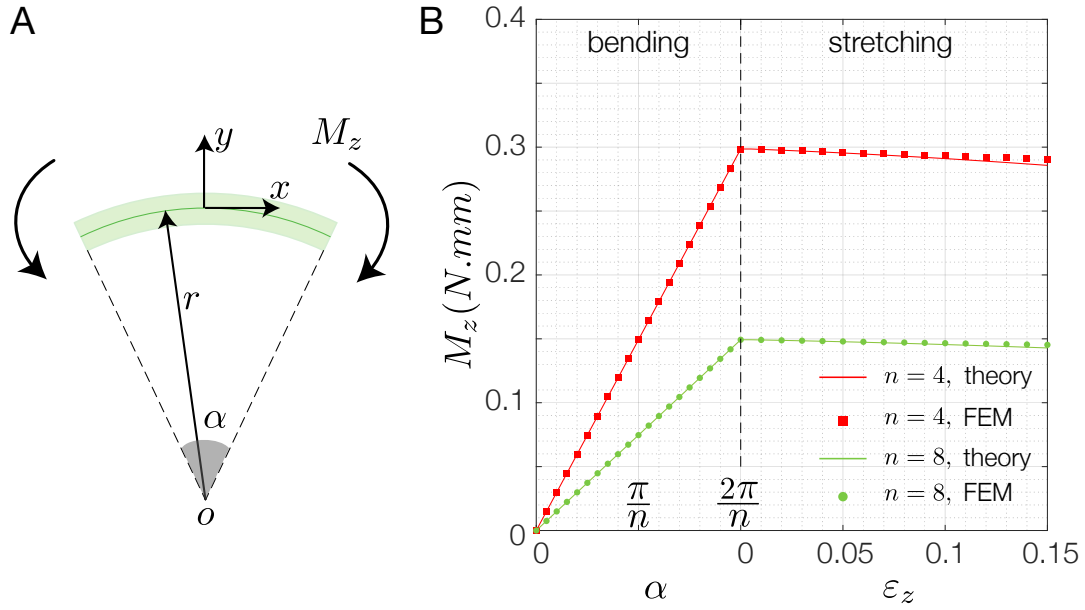


Fig. S13. Validation of the periodic boundary conditions by comparing analytical solutions [Eq. S12] and FE simulations for a solid sheet that is first rolled into a (portion of) a cylinder and then stretched. (A) Schematic of the unit cell. (B) Comparison between FE and analytical results for $n=4$ and 8.

where $\epsilon_x = y/r$ is the circumferential strain, $r = L/\alpha$ being the radius of the cylinder. It follows that the bending moment $M_z^{bending}$ required to bend the flat cell into a curved one is given by

$$M_z^{bending} = \int_{-t/2}^{t/2} \sigma_x H y dy = \frac{E H t^3 \alpha}{12L(1-\nu^2)}. \quad [S11]$$

As for the stretching process, because of the Poisson's effect, we expect the sheet to shrink circumferentially, so that

$$\epsilon_x = \frac{y}{r} - \nu \epsilon_z, \quad \epsilon_y = -\nu \epsilon_z \quad [S12]$$

ϵ_z denoting the applied axial stretch. Moreover, during stretching $\alpha = 2\pi/n$ and $r = nL/2\pi$ (n being the number of unit cell along the circumference). Consequently, the bending moment during the stretching process reads:

$$M_z^{stretching} = \int_{-t(1-\nu\epsilon_z)/2}^{t(1-\nu\epsilon_z)/2} \sigma_x H (1 + \epsilon_z) y dy = \frac{\pi E H t^3 (\epsilon_z + 1) (1 - \nu \epsilon_z)^3}{6nL(1-\nu^2)}. \quad [S13]$$

In Fig. S13C we compare analytical (Eqs. S11 and S13) and FE results (using Eqs. S7 and Eqs. S4 with Eq. S8 and Eq. S9) for $n=4$ and 8. We find a great agreement between the two sets of data, confirming the validity of our numerical analysis.

Curved kirigami sheets. To investigate the effect of the residual stresses generated during rolling on the mechanical response of our kirigami cylinders, we also performed simulations on initially curved (stress-free) models. The curved models are created in SolidWorks (Version 2016) by wrapping a flat cell around a curved sector of a cylindrical surface with radius $r = Ln/(2\pi)$. To stretch them axially, we then apply the following periodic boundary conditions to their *left* and the *right* edges:

$$\begin{aligned}
u_{\rho}^{R_i} &= u_{\rho}^{L_i}, \\
u_{\phi}^{R_i} &= u_{\phi}^{L_i}, \\
u_z^{R_i} &= u_z^{L_i}, \\
\theta_{\rho}^{L_i} &= \theta_{\rho}^{R_i} = 0, \\
\theta_{\phi}^{L_i} &= \theta_{\phi}^{R_i}, \\
\theta_z^{L_i} &= \theta_z^{R_i} = 0, \quad i = 1, 2, \dots, N.
\end{aligned}
\tag{S14}$$

As for the *top* and *bottom* edges, we apply the same periodic boundary used for the case of the rolled kirigami sheets.

Additional numerical results are provided in Figs. [S14-S21](#).

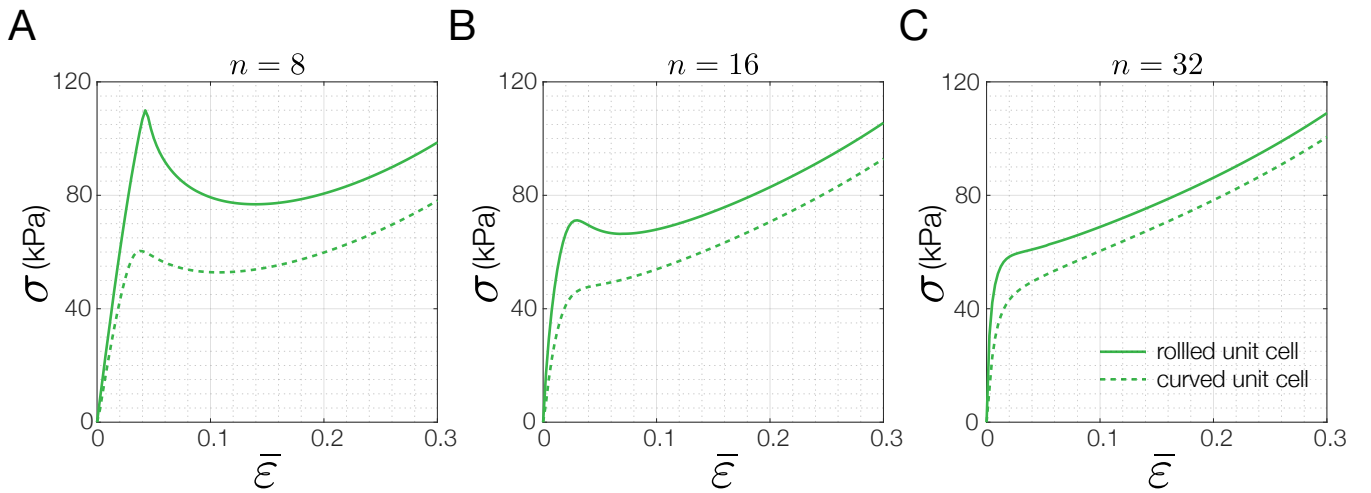


Fig. S14. Comparison between the stress-strain curve of curved and rolled unit kirigami sheets with triangular cuts. We consider unit cells with $l = 12\text{mm}$ and $\delta = 0.75\text{mm}$ and use (A) $n = 8$, (B) $n = 16$ and (C) $n = 32$. We observe that for small n (i.e. large curvature) the rolled kirigami sheets are significantly stiffer than the initially curved ones. However, as the number of units along the circumference increases their responses converge to each other. Also, we find that for the rolled kirigami sheets the overshoot in stress-strain curve is more pronounced than for initially curved ones.

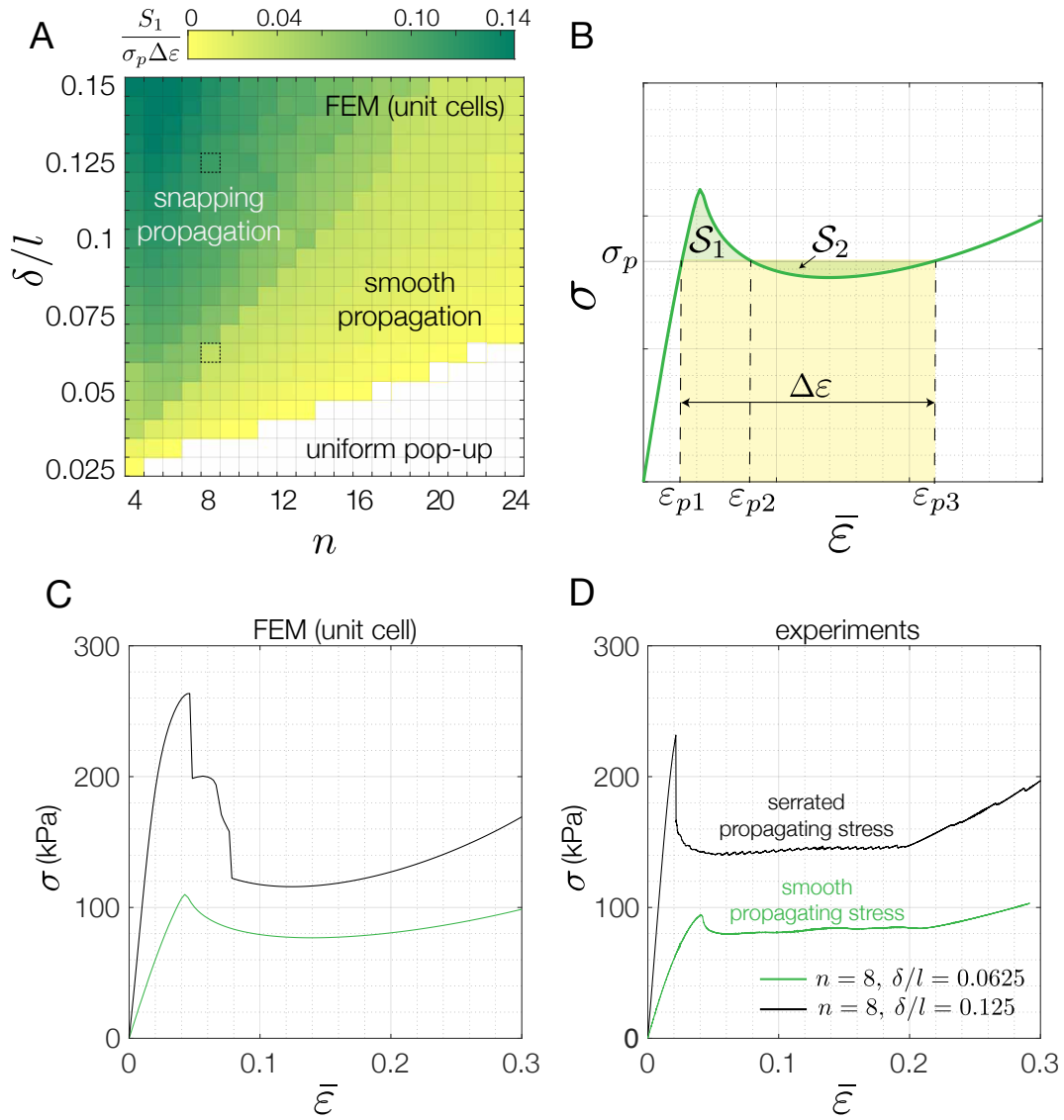


Fig. S15. (A) Phase diagram for kirigami shells with triangular cut pattern. The color indicates the energy barrier S_1 (see shaded green area in B) normalized by the total energy required for phase transition (i.e. $\sigma_p \Delta \epsilon$). The white region represents uniform pop-up. This plot is obtained by simulating the response of 441 rolled unit cells. The type of behavior is determined based on the obtained stress-strain curve. If the stress monotonically increases as a function of the strain, a uniform pop-up is triggered; otherwise a propagative instability. (B) Schematic strain-stress curve of a unit cell of a kirigami shell indicating the energy barrier S_1 , propagation stress σ_p obtained by the condition $S_1 = S_2$, strain increment required for phase transition $\Delta \epsilon$, two stable strains at unpopped (ϵ_{p1}) and popped ($\epsilon_{p3} = \epsilon_{p1} + \Delta \epsilon$) states and the intermediate unstable strain ϵ_{p2} . (C) FE stress-strain curves obtained by simulating two rolled unit cells ($n = 8$, $L = 12$ mm) with triangular cuts indicated in phase diagram (A) with dashed squares and characterized by FE $\delta/l = 0.0625$ and $\delta/l = 0.125$. (D) Experimental stress-strain curves for two kirigami shells built using the unit cells considered in C. Note that the sharp drop in load found in the stress-strain curve of the unit cell with $\delta/l = 0.125$ results in a discrete sequence of small drops during propagation of pop-ups in the finite-sized structure, each corresponding to the opening of one row of cuts. For such snapping propagation regime we expect a fraction of energy to be dissipated, so that the use of Maxwell's rule (which is based on the assumption of a conservative system) is not rigorous.

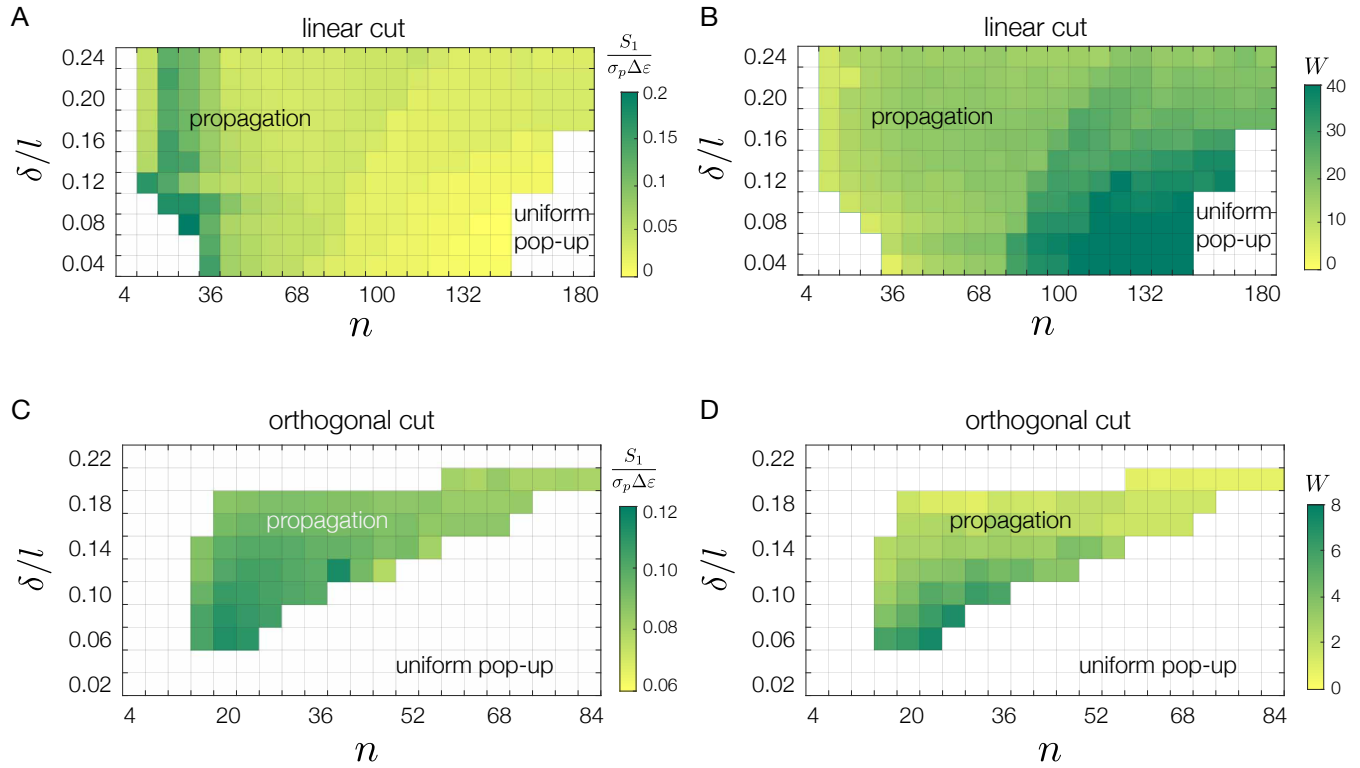


Fig. S16. Phase diagrams for kirigami shells with (A, B) linear and (C, D) orthogonal cut patterns obtained by simulating respectively 253 and 231 rolled unit cells. The color in A and C indicates the energy barrier S_1 (see shaded green area in Fig. S15B) normalized by the total energy required for phase transition (i.e. $\sigma_p \Delta \varepsilon$) while in B and D, the color shows W the width of the transition zone in the unit of number of units. The white region represents uniform pop-up. These plots are obtained as described in the caption of Fig. S15. Note that, since the response of the linear pattern is very sensitive to imperfection, the phase diagram shown in (A) is obtained by imposing an initial imperfection with magnitude equal to $0.1t$. Moreover, since for most configurations the energy barrier is very small, we expect only a limited number of them (characterized by large S_1) to exhibit a well visible propagation of pop-ups.

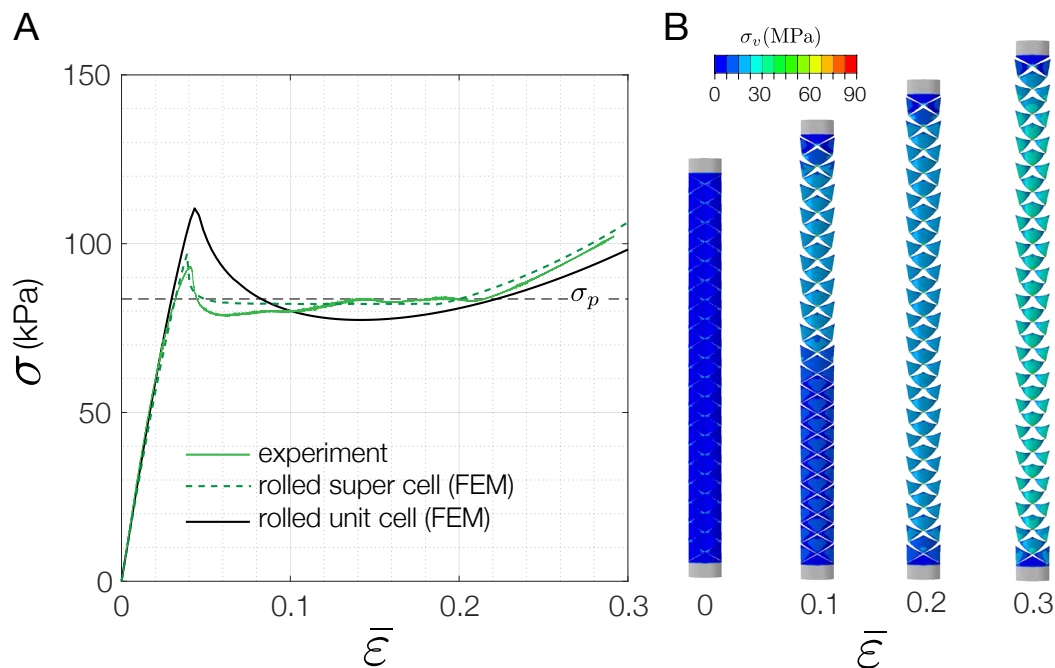


Fig. S17. (A) Stress-strain response for a kirigami shell with triangular pattern characterized by $l = 12$ mm and $\delta = 0.75$ mm. Results from FE simulations conducted on a rolled 20×1 super-cell are compared to experiments and to the numerical predictions obtained for the corresponding unit cell. Excellent agreement between experiments and FE simulations is found. (B) Snapshots of the deformed super-cell at different applied strain $\bar{\epsilon}$. In the snapshots we also show the *von Mises* stress distributions.

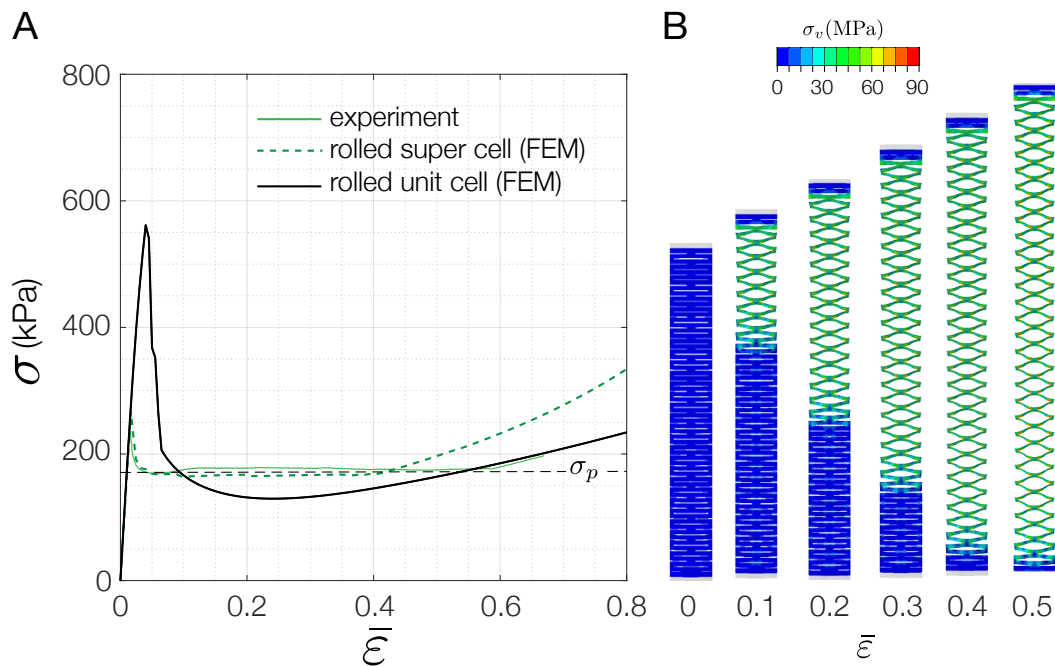


Fig. S18. (A) Stress-strain response for a kirigami shell with linear pattern characterized by $l = 12$ mm and $\delta/l = 0.2$. Results from FE simulations conducted on a rolled 20×1 super-cell are compared to experiments and to the numerical predictions obtained for the corresponding unit cell. Excellent agreement between experiments and FE simulations is found. (B) Snapshots of the deformed super-cell at different applied strain $\bar{\epsilon}$. In the snapshots we also show the *von Mises* stress distributions.

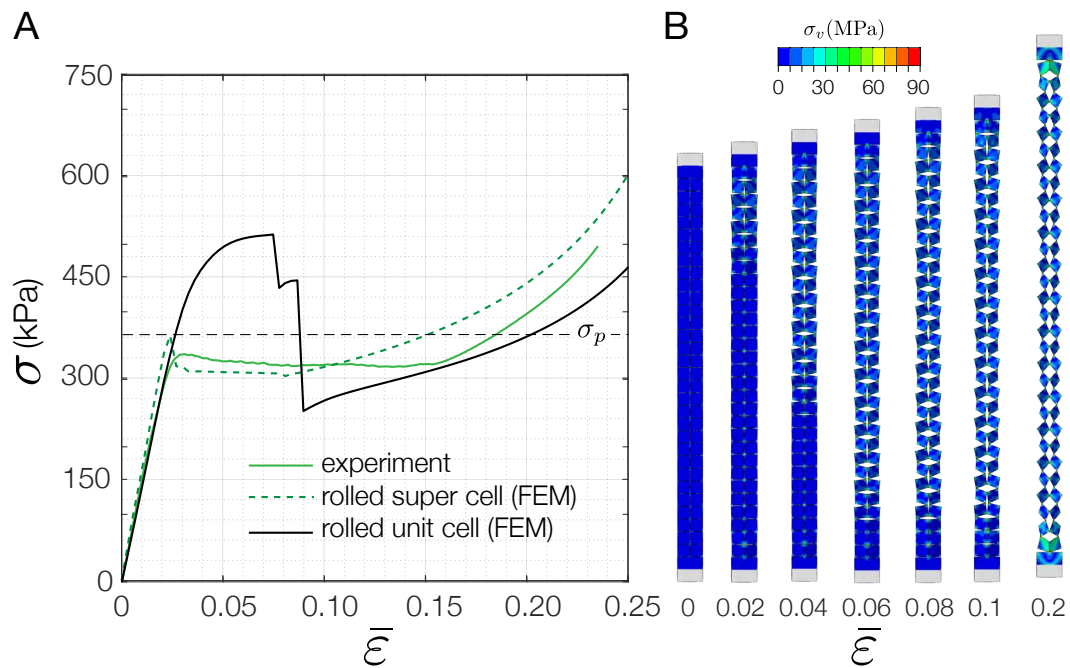


Fig. S19. (A) Stress-strain response for a kirigami shell with orthogonal pattern characterized by $l = 6$ mm and $\delta/l = 0.08$. Results from FE simulations conducted on a rolled 20×1 super-cell are compared to experiments and to the numerical predictions obtained for the corresponding unit cell. Excellent agreement between experiments and FE simulations is found. (B) Snapshots of the deformed super-cell at different applied strain $\bar{\epsilon}$. In the snapshots we also show the *von Mises* stress distributions.

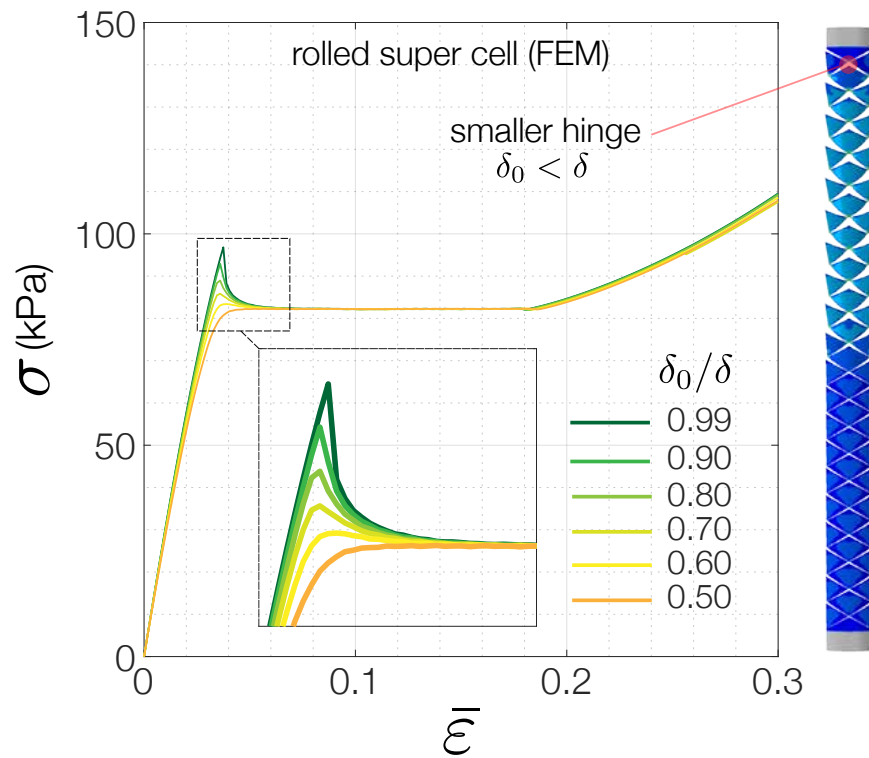


Fig. S20. The effect of the imperfection size on the stress-strain behavior of kirigami shell is investigated by conducting FEM simulations on super-cells with a triangular cut pattern characterized by $\delta/l = 0.0625$, $l = 12\text{mm}$ and $n = 8$. In our models the size of the hinge in the top unit cell is reduced to $\delta_0 < \delta$. We find that as δ_0/δ increases the overshoot in the stress-strain curve decreases and eventually vanishes for $\delta_0/\delta=0.5$. By contrast, the propagation stress σ_p is not affected by δ_0/δ .

B. Theoretical model. Both our experiments and our FE simulations show that in thin cylindrical kirigami shells subjected to tensile loading the buckling induced pop-up process initially localizes near an imperfection and then, as the deformation is increased, progressively spreads through the cylinder at constant stress. Moreover, our FE simulations indicate that the stress-strain response of a rolled kirigami unit cell is non-monotonic, characterized by a peak, a subsequent drop in load and final stiffening (see Fig. 3B of the main text). Guided by these observations, here we develop models to characterize the behavior of our kirigami structures.

Maxwell construction. Maxwell construction (10) applied to the stress-strain response of a unit cell enables us to identify several key parameters that characterize the behavior of our curved kirigami shell. Specifically, by equating the area of the two lobes formed by the $\sigma(\varepsilon)$ curve (i.e. by imposing $\mathcal{S}_1 = \mathcal{S}_2$) we can identify (i) the propagation stress σ_p , (ii) the energy barrier \mathcal{S}_1 and (iii) the critical strains ε_{p1} , ε_{p2} and ε_{p3} (see Fig. S21). While for $\bar{\varepsilon} < \varepsilon_{p1}$ the structure deforms homogeneously and all triangular features are unpopped, for $\varepsilon_{p1} < \bar{\varepsilon} < \varepsilon_{p3}$ the pop-up process initiated at the top end of the sample spreads towards the other end. However, it is important to note that Maxwell construction does not provide any information on the width and the shape of the transition zone. This motivates the derivation of the more detailed and comprehensive model described below.

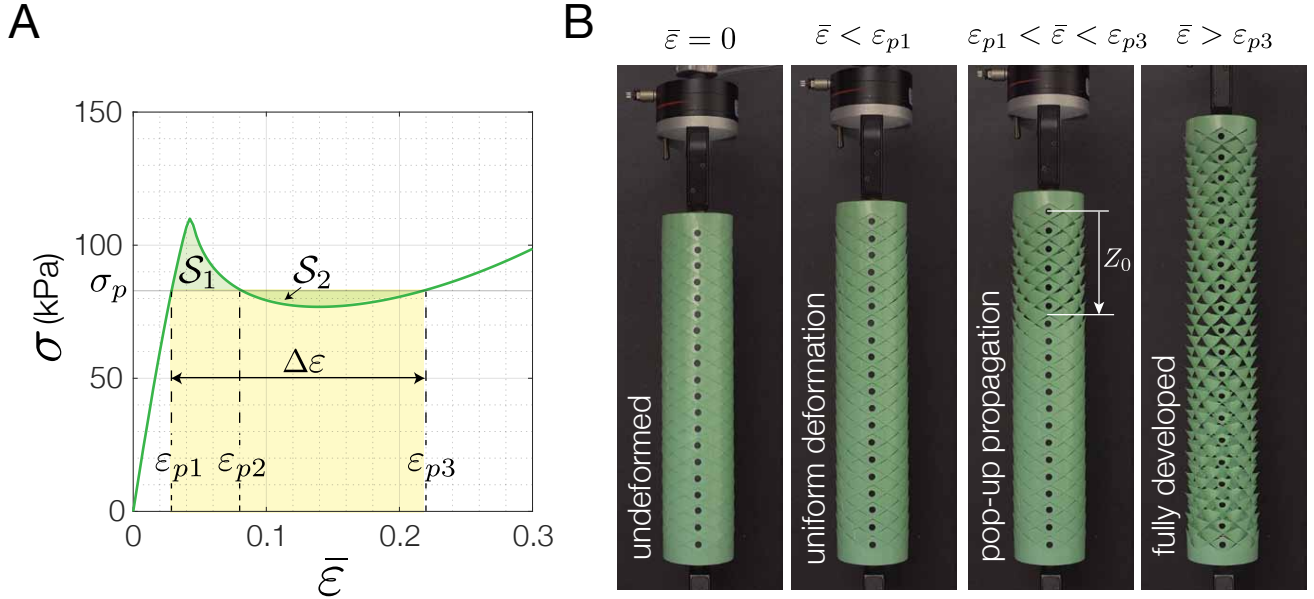


Fig. S21. (A) Typical stress-strain curve for a rolled kirigami unit cell. Several parameters can be identified from Maxwell construction (i.e. by imposing $\mathcal{S}_1 = \mathcal{S}_2$). (B) Experimental images of a kirigami shell fabricated by rolling a sheet with a triangular pattern characterized by $\delta/l = 0.0625$ (with $l = 12$ mm and $n = 8$ unit cells along the circumference) at $\bar{\varepsilon} = 0$ (before the test starts), $\bar{\varepsilon} < \varepsilon_{p1}$ (before the pop-up process starts), $\varepsilon_{p1} < \bar{\varepsilon} < \varepsilon_{p3}$ (during propagation of pop-ups) and $\bar{\varepsilon} > \varepsilon_{p3}$ (after all triangular features popped-up).

Detailed model. To predict the strain distribution during the propagation of the pop-ups, we use a 1D array of non-linear springs (see Fig. S22). In our model the response of the i -th spring is described by

$$F_i(u_i, u_{i+1}) = nLt \times \sigma(\varepsilon_i), \quad \text{with } \varepsilon_i = \frac{u_{i+1} - u_i}{H}, \quad [\text{S15}]$$

where $\sigma(\varepsilon_i)$ is the non-linear stress-strain response of the unit cell and u_i and u_{i+1} denote the axial displacement at the two ends of the spring.

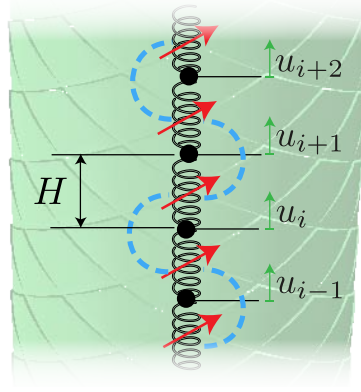


Fig. S22. The response of our kirigami structures is captured using a 1D array of non-linear springs connected in series. To accurately capture the effect of strain gradient we introduce an additional term (represented by the blue dashed lines in the schematic) that connects the response of the i -th spring to that of the two neighboring ones.

It follows that for a system comprising a N springs the total strain energy is given by

$$U = \sum_{i=1}^N \int_0^{u_{i+1}-u_i} F_i d(u_{i+1} - u_i) = \sum_{i=1}^N nLt \int_0^{u_{i+1}-u_i} \sigma \left(\frac{u_{i+1} - u_i}{H} \right) d(u_{i+1} - u_i), \quad [\text{S16}]$$

from which the equilibrium equation can be derived as

$$\frac{\partial U}{\partial u_i} = 0, \quad \text{for } i = 1, \dots, N. \quad [\text{S17}]$$

To test the ability of our discrete model to capture the response of our kirigami structures, we focus on a kirigami shell with $n = 8$ and triangular cuts characterized by $\delta/l = 0.0625$. We first use FE analyses to determine the stress-strain behavior of the unit cell (see Fig. S23A). Then, we use both FE analyses and our discrete model based on Eq. S16 to investigate the response of a cylindrical shell comprising two rows of unit cells (i.e. $N = 2$) when subjected to two different loading conditions, case #1 and case #2 (see Fig. S23B). For case #1, we stretch the two unit cells homogeneously (i.e. we impose $\varepsilon_1 = \varepsilon_2$ and progressively increase ε_1), whereas for Case #2 we stretch the first unit cell, while keeping the second one closed (i.e. we set $\varepsilon_2 = 0$ and progressively increase ε_1), inducing a highly inhomogeneous deformation. As it can be seen in Figs. S23C and D, the inhomogeneous deformation (i.e. the strain gradient) of case #2 makes the structure significantly stiffer - a feature that cannot be captured by our simple model.

To properly account for the effect of the strain gradient, which significantly affects the response of our system given the strong coupling between its unit cells, we modify the strain energy given in Eq. S16 to

$$U = \sum_{i=1}^N nLt \int_0^{u_{i+1}-u_i} \sigma \left(\frac{u_{i+1} - u_i}{H} \right) d(u_{i+1} - u_i) + \sum_{i=2}^N \frac{1}{2} nLtG (u_{i+1} - 2u_i + u_{i-1})^2. \quad [\text{S18}]$$

where the last term is introduced to capture the effect of the strain gradient (8, 9) (see Fig. S22B). Note that the coefficient G in Eq. S18 can be easily determined using the two FE simulations shown

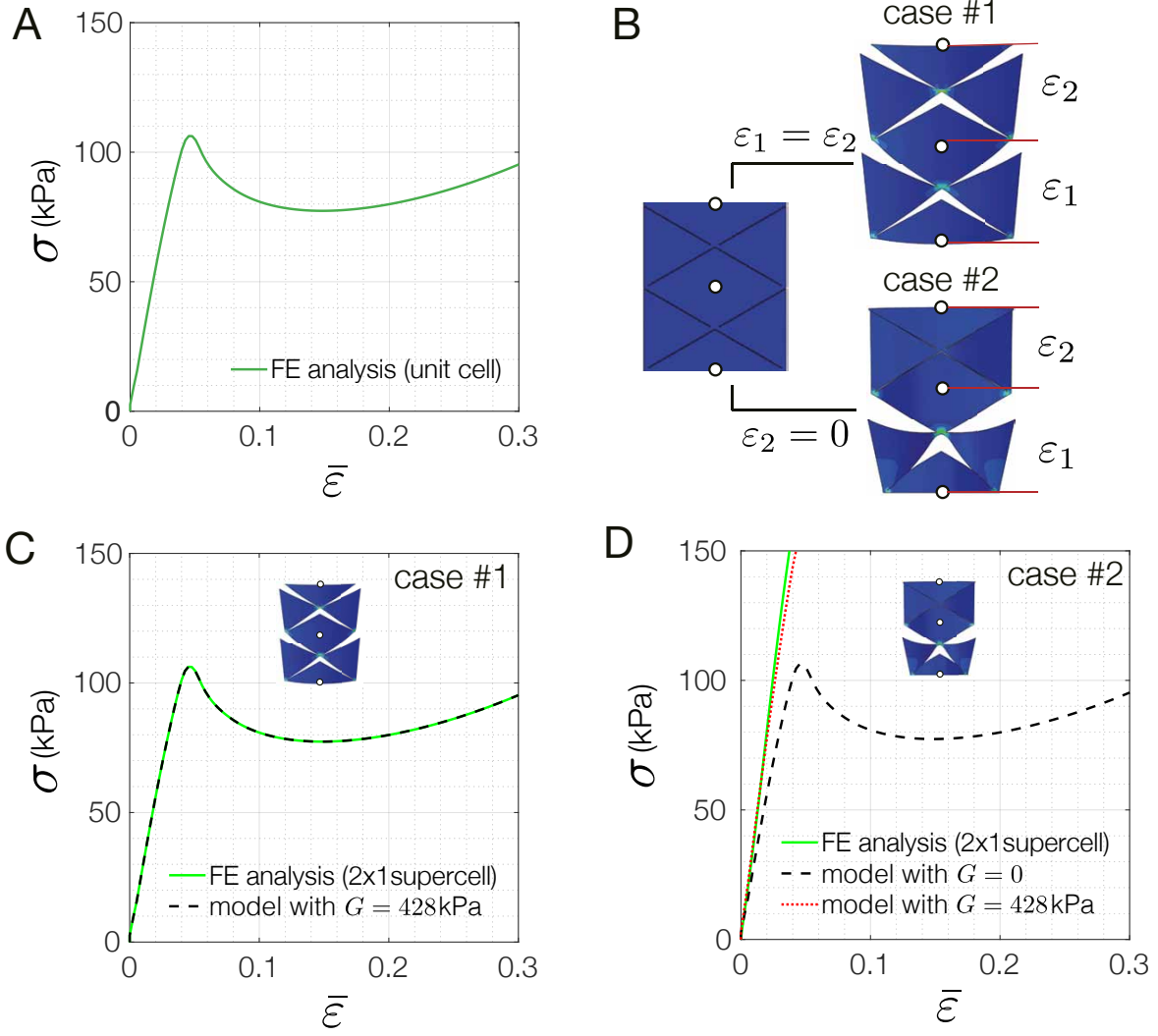


Fig. S23. (A) Stress-strain curve for a unit cell of a kirigami shell with $n=8$ and $\delta/l = 0.0625$ as predicted by our FE analysis. (B) We simulate the response of a super-cell comprising 2×1 unit cells when: (case #1) the two unit cells are stretched homogeneously (i.e. we impose $\varepsilon_1 = \varepsilon_2$ and progressively increase ε_1) and (case #2) the first unit cell is stretched while the second one is kept closed (i.e. we set $\varepsilon_2 = 0$ and progressively increase ε_1). (C) The response of the structure for case #1 obtained via FE analysis is nicely captured by both the model with $G = 0$ and $G = 428$ kPa. (D) The response of the structure for case #1 obtained via FE analysis is not captured by the model with $G = 0$, whereas is nicely captured by the model with $G = 428$ kPa, motivating the introduction of the strain gradient term.

in Fig. S23. More specifically, since the initial stiffness K predicted using Eq. S18 for Case #1 and Case #2 is given by

$$\begin{aligned}
 K_{Case\ #1} &= \left. \frac{\partial^2 U_{Case\ #1}}{\partial (u_2 - u_1)^2} \right|_{u_1=u_2=0} = \left. \frac{nLt}{H} \frac{\partial \sigma(\varepsilon)}{\partial \varepsilon} \right|_{\varepsilon=0}, \\
 K_{Case\ #2} &= \left. \frac{\partial^2 U_{Case\ #2}}{\partial (u_2 - u_1)^2} \right|_{u_1=u_2=0} = \left. \frac{nLt}{H} \frac{\partial \sigma(\varepsilon)}{\partial \varepsilon} \right|_{\varepsilon=0} + nLtG,
 \end{aligned} \tag{S19}$$

it follows that

$$G = \frac{K_{Case\ #2} - K_{Case\ #1}}{nLt}. \tag{S20}$$

In Figs. S23C and D we compare the results of our discrete model based on Eq. S18 with those

obtained via FE analyses. We find that using $G = 428$ kPa (value determined using Eq. S20) the model captures very well the response of the structure for both loading cases, indicating that the coupling constant G should be included in the model to correctly capture the response of our system. On the other hand, it is interesting to note that if a structure consists of units that are not strongly coupled so that $K_{Case\#1} - K_{Case\#2} \rightarrow 0$, then $G \rightarrow 0$ and the term introduced to capture the effect of strain gradient vanishes.

Having established a simple discrete model capable of capturing the non-linear response of our kirigami structures, we now use it to investigate the characteristics of the triggered propagative instability. To this end, since our experiments indicate that the propagation of the instability-induced pop-up process occurs at a constant axial stress σ_p , we write the total potential energy of the system as,

$$\begin{aligned} \Pi &= U - F_p(u_{N+1} - u_1) \\ &= \sum_{i=1}^N nLt \int_0^{u_{i+1}-u_i} \sigma\left(\frac{u_{i+1}-u_i}{H}\right) d(u_{i+1}-u_i) + \sum_{i=2}^N \frac{1}{2} nLtG (u_{i+1} - 2u_i + u_{i-1})^2 - F_p(u_{N+1} - u_1), \end{aligned} \quad [\text{S21}]$$

with

$$F_p = nLt\sigma_p. \quad [\text{S22}]$$

We then derive the equilibrium equations by imposing

$$\frac{\partial \Pi}{\partial u_i} = 0, \quad \text{for } i = 1, \dots, N. \quad [\text{S23}]$$

and obtain

$$\begin{aligned} \sigma\left(\frac{u_{i+1}-u_i}{H}\right) - \sigma\left(\frac{u_i-u_{i-1}}{H}\right) \\ - G[u_{i+2} - 4u_{i+1} + 6u_i - 4u_{i-1} + u_{i-2}] = 0, \quad \text{for } i = 3, \dots, N-1 \end{aligned} \quad [\text{S24}]$$

which can be rewritten in terms of the local strain $\varepsilon_i = (u_{i+1} - u_i)/H$ as

$$\mathcal{E}_i = \sigma(\varepsilon_i) - \sigma(\varepsilon_{i-1}) - G(\varepsilon_{i+1} - 3\varepsilon_i + 3\varepsilon_{i-1} - \varepsilon_{i-2}) = 0, \quad \text{for } i = 3, \dots, N-1 \quad [\text{S25}]$$

Next, we introduce a continuous function $\varepsilon(Z)$, which interpolates the discrete variable ε_i as

$$\varepsilon(Z = iH) = \varepsilon_i, \quad [\text{S26}]$$

where Z denotes the position along the structure. Using Taylor expansion, the strains $\varepsilon_{i\pm 1}$ and $\varepsilon_{i\pm 2}$ can then be expressed as

$$\varepsilon_{i+p} = \varepsilon(iH) + pH \frac{d\varepsilon(iH)}{dZ} + \frac{p^2 H^2}{2} \frac{d^2 \varepsilon(iH)}{dZ^2} + \frac{p^3 H^3}{6} \frac{d^3 \varepsilon(iH)}{dZ^3} + \mathbf{O}\left(\frac{d^4 \varepsilon(iH)}{dZ^4}\right), \quad [\text{S27}]$$

with $p = -2, -1, 1$ and 2 . By substituting Eqs. S27 into

$$\mathcal{E}_{i+1} + \mathcal{E}_i = \sigma(\varepsilon_i) - \sigma(\varepsilon_{i-1}) - G(\varepsilon_{i+2} - 2\varepsilon_{i+1} + 2\varepsilon_{i-1} - \varepsilon_{i-2}) = 0 \quad [\text{S28}]$$

and retaining terms up to the third order, we obtain

$$GH^2 \frac{d^3 \varepsilon}{dZ^3} - \frac{d\sigma(\varepsilon)}{dZ} = 0, \quad [\text{S29}]$$

which we integrate with respect to Z to get

$$GH^2 \frac{d^2\varepsilon}{dZ^2} - \sigma(\varepsilon) + C_1 = 0, \quad [\text{S30}]$$

where C_1 is an integration constant. If we assume that at $Z \rightarrow -\infty$ the structure is unpopped (so that $d^2\varepsilon/dZ^2|_{-\infty} = 0$) and define ε_{p1} as the strain experienced by the unpopped unit cells when subjected to a constant stress σ_p (i.e. $\varepsilon(Z \rightarrow -\infty) = \varepsilon_{p1}$, where ε_{p1} is the smallest root of $\sigma(\varepsilon) - \sigma_p = 0$), we find that

$$C_1 = \sigma(\varepsilon_{p1}) = \sigma_p. \quad [\text{S31}]$$

Substitution of Eq. S31 into Eq. S30 yields

$$GH^2 \frac{d^2\varepsilon}{dZ^2} = \sigma(\varepsilon) - \sigma_p, \quad [\text{S32}]$$

which can be solved to obtain the spatial profile of the strain, $\varepsilon(Z)$, for a given σ_p .

Next, to gain more insight into the response of our kirigami structures, we multiply Eq. S32 by $d\varepsilon/dZ$ and integrate with respect to Z to get

$$\frac{1}{2}GH^2 \left(\frac{d^2\varepsilon}{dZ^2} \right)^2 = - \int_0^\varepsilon [\sigma(\varepsilon') + \sigma_p] d\varepsilon' \quad [\text{S33}]$$

which can be viewed as the sum of the kinetic energy (with respect to the pseudo-time Z) and the potential energy of a fictitious particle of mass GH^2 (13). Thus, the solution $\varepsilon(Z)$ of Eq. S32 describes the motion of such particle in the potential

$$V_{eff}(\varepsilon) = - \int_0^\varepsilon [\sigma(\varepsilon') - \sigma_p] d\varepsilon'. \quad [\text{S34}]$$

Specifically, the existence of propagation of pop-ups requires a V_{eff} with two stable configurations (located at ε_{p1} and ε_{p3}) characterized by the same energy level. Under these conditions, a fictitious particle leaving the first peak at rest can reach the second one with a vanishing "velocity" $d\varepsilon/dZ$ and this corresponds to a transition that brings each unit cell from ε_{p1} and ε_{p3} . Focusing on the kirigami unit cells investigated in this study, we find that, if the stress-strain curve of the unit cell is monotonic (as for our flat unit cells - see Fig. S24A), V_{eff} has a single stable configuration (see Fig. S24B) and propagation of pop-ups cannot exist. By contrast, if the stress-strain curve is non-monotonic (and characterized by an up-down-up behavior - see Fig. S24C) and σ_p is chosen so that the equation $\sigma(\varepsilon) - \sigma_p = 0$ has three real roots, V_{eff} has two stable configurations (see Fig. S24C) located at ε_{p1} and ε_{p3} (see Fig. S24D). However, these two configurations are characterized by the same energy only when σ_p corresponds to the Maxwell stress (i.e. the stress for which $\mathcal{S}_1 = \mathcal{S}_2$) - an observation that confirms the validity of our model. Inspection of Eq. S33 also provides insights on the width of the transition zone. More specifically, since the motion of the fictitious particles gets slower as its mass GH^2 increases, we expect the transition zone to become wider for larger GH^2 (i.e. for structures characterized by a larger coupling constant G). Therefore, given a specific non-monotonic stress strain curve of the unit cell $\sigma(\varepsilon)$, Eq. S32 can be numerically solved to obtain the strain distribution within the structure during the propagation of the pop-ups.

Finally, we validate the ability of our model to capture the response of our kirigami structures by comparing the evolution of the strain along the cylindrical kirigami shells as predicted by our model and measured in experiments at different level of applied strain for shells with triangular pattern

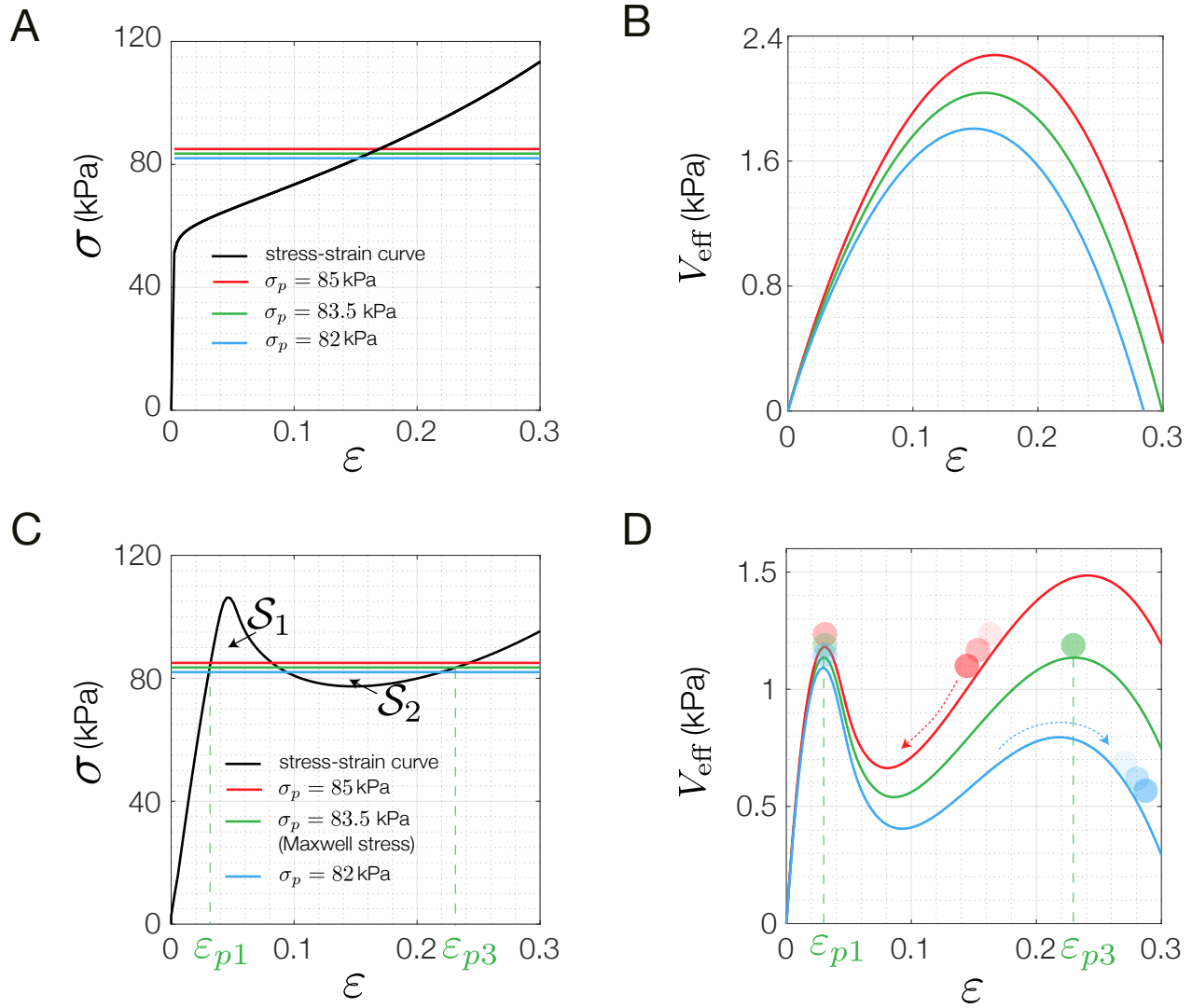


Fig. S24. (A) Stress-strain curve of a flat unit cell with triangular cuts characterized by $\delta/l = 0.0625$ as obtained via FE analysis. (B) Corresponding potential energy V_{eff} as a function of applied strain ε for three different σ_p (note that the color of the curves corresponds to the σ_p indicated in A). (C) Stress-strain curve of a rolled unit cell with $n=8$ and triangular cuts characterized by $\delta/l = 0.0625$ as obtained via FE analysis. (D) Corresponding potential energy V_{eff} as a function of applied strain ε for three different σ_p (note that the color of the curves corresponds to the σ_p indicated in A)

(with $\delta/l = 0.0625$ and $n = 8$ - Fig. S25A), linear pattern (with $\delta/l = 0.2$ and $n = 20$ - Fig. S25B) and orthogonal pattern (with $\delta/l = 0.08$ and $n = 20$ - Fig. S25C). Note that the model predictions are obtained by numerically integrating Eq. S32 with $\sigma(\varepsilon)$ predicted by our FE simulations on the unit cell and σ_p equal to the Maxwell stress. Moreover, since the solution of Eq. S32 is translational invariant with respect to Z , the position of the propagation front Z_0 (see Fig. S21B) for a given applied strain $\bar{\varepsilon}$ can be determined from the compatibility condition

$$\bar{\varepsilon} = \frac{1}{Z_q - Z_p} \int_{Z_p}^{Z_q} \varepsilon(Z - Z_0) dZ. \quad [\text{S35}]$$

where, to minimize boundary effects, we choose $(p, q) = (3, 18)$, $(5, 55)$ and $(1, 30)$ for structures with triangular, linear and orthogonal patterns, respectively. In Fig. S25 we find a very nice agreement between the experimental results and the predictions of our model, with our model

correctly predicting the very different widths and amplitudes of the transition zones for the three structures as well as their position as a function of the applied deformation.

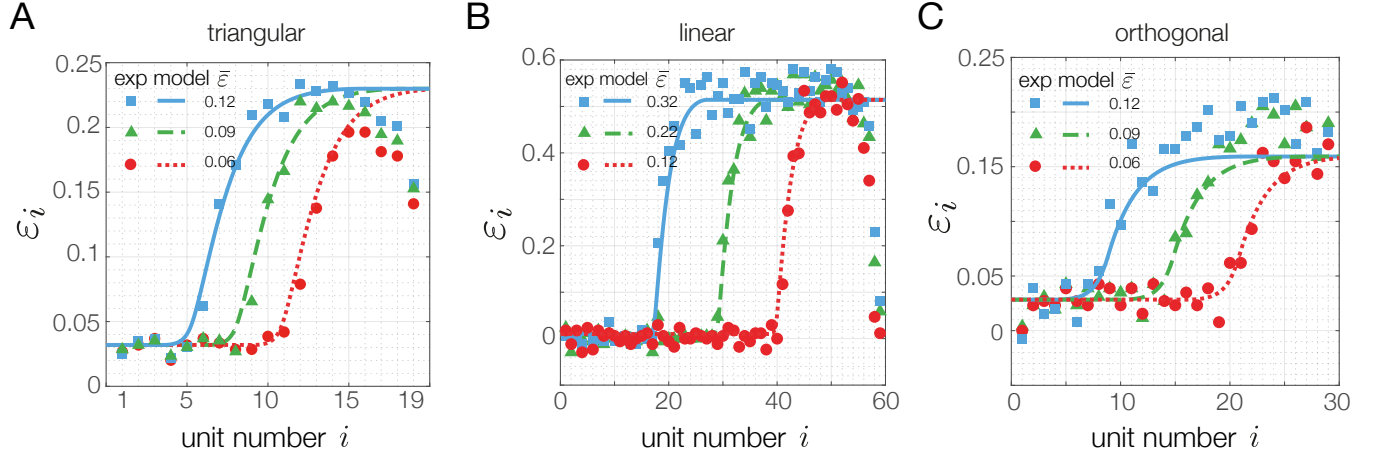


Fig. S25. Comparison between the evolution of the strain along the cylindrical kirigami shells as measured in experiments and obtained by numerically integrating Eq. S32 for (a) a triangular pattern with $\delta/l = 0.0625$ and $n = 8$, (b) a linear pattern with $\delta/l = 0.2$ and $n = 20$ and (c) an orthogonal pattern with $\delta/l = 0.08$ and $n = 20$.

Special case with analytical solution. While Eq. S36 is nonlinear, it is interesting to note that it admits analytical solution if the stress-strain curve of a unit cell is described by a third order polynomial,

$$\sigma(\varepsilon) = B_1\varepsilon + B_2\varepsilon^2 + B_3\varepsilon^3. \quad [\text{S36}]$$

Substitution of Eq. S36 into the continuum governing equation Eq. S32 yields,

$$\frac{d^2\varepsilon}{dZ^2} = \frac{B_1\varepsilon + B_2\varepsilon^2 + B_3\varepsilon^3 - \sigma_p}{GH^2}, \quad [\text{S37}]$$

which is a Klein-Gordon equation with quadratic and cubic nonlinearities (12). Such equation yields analytical solution of the form

$$\varepsilon(Z) = \varepsilon_{p1} + \frac{\Delta\varepsilon}{2} \left[1 + \tanh\left(\frac{Z - Z_0}{W}\right) \right], \quad [\text{S38}]$$

where ε_{p1} and $\varepsilon_{p1} + \Delta\varepsilon$ denote the strain experienced by the unit cells in the closed/unpopped and open/popped configuration, respectively, W is the width of the transition zone and Z_0 provides the position of such transition zone. By substituting the solution S38 into Eq. S32 we find that the latter is identically satisfied only if

$$\Delta\varepsilon = \frac{2\sqrt{B_2^2 - 3B_1B_3}}{\sqrt{3B_3}}, \quad \varepsilon_{p1} = -\frac{\Delta\varepsilon}{2} - \frac{B_2}{3B_3}, \quad W = H\sqrt{\frac{6GB_3}{B_2^2 - 3B_1B_3}}. \quad [\text{S39}]$$

At this point it is also important to point out that the strain distribution defined by Eq. S38 exists only if $\Delta\varepsilon$, W and ε_{p1} are real valued, a condition that is satisfied only if

$$B_2^2 - 3B_3 > 0, \quad \text{and} \quad G > 0. \quad [\text{S40}]$$

Moreover, an explicit expression for the propagation stress can be obtained by substituting Eq. S39 into Eq. S36

$$\sigma_p = \sigma(\varepsilon_{p1}) = \frac{2B_2^3 - 9B_1B_2B_3}{27B_3^2}. \quad [\text{S41}]$$

and the position of the transition zone Z_0 is determined by introducing Eq. S38 into Eq. S35

$$\bar{\varepsilon} = \varepsilon_{p1} + \frac{\Delta\varepsilon}{2} + \frac{W\Delta\varepsilon}{Z_q - Z_p} \left\{ \log \left[\cosh \left(\frac{Z_q - Z_0}{W} \right) \right] - \log \left[\cosh \left(\frac{Z_p - Z_0}{W} \right) \right] \right\}. \quad [\text{S42}]$$

Finally, we note that, since the energy barrier \mathcal{S}_1 is given by

$$\mathcal{S}_1 = \int_{\varepsilon_{p1}}^{\varepsilon_{p2}} (B_1\varepsilon_i + B_2\varepsilon_i^2 + B_3\varepsilon_i^3) d\varepsilon_i - \sigma_p(\varepsilon_{p2} - \varepsilon_{p1}) = \frac{(B_2^2 - 3B_1B_3)^2}{36B_3^3}, \quad [\text{S43}]$$

where ε_{pi} (with $i = 1, 2$ and 3) denote the three roots of

$$B_1\varepsilon + B_2\varepsilon^2 + B_3\varepsilon^3 = \sigma_p, \quad [\text{S44}]$$

the width of the transition zone can be expressed as,

$$W = \sqrt{\frac{G}{\sqrt{B_3\mathcal{S}_1}}}. \quad [\text{S45}]$$

Eq. S45 clearly show that the width of the transition zone W is determined by the balance between G (which captures the level of coupling between the unit cells) and \mathcal{S}_1 (which represent the energy barrier to overcome for the pop-up process to propagate). The larger is the coupling or the smaller is the energy barrier, the larger is the width of the transition zone.

Movie S1. Propagation of instability in a long party balloon.

During inflation a long party balloon, first expands diametrically in a uniform fashion. However, at some value of pressure, the deformation localizes near an imperfection forming a bulge. Finally, as more compressed gas is made available, the bulge grows to a well defined diameter and then stops growing diametrically and starts growing in length. Inflation of a long party balloon is an example of instability propagation.

Movie S2. Fabrication of kirigami shells.

Fabrication of a kirigami shell: (i) the double-sided adhesive is laser cut into the desired shape; (ii) the polyester sheet is attached to the adhesive layer and the kirigami pattern is laser cut; (iii) very thin adhesive black markers are attached to the sheet to track the deformation during testing; (iv) the two edges of the sheet are attached together using needles to facilitate alignment; (v) two bolted acrylic caps are laser cut; (vi) the caps are glued to the cylinder ends.

Movie S3. Kirigami with triangular cuts: tensile response of sheet vs shell

Comparison between tensile deformation of three kirigami structures with triangular cuts: (left) a flat kirigami sheet characterized by 2×20 units with $\delta/l = 0.0625$, (middle) a kirigami shell characterized by 8×20 units with $\delta/l = 0.0333$ and (right) a kirigami shell characterized by 8×20 units with $\delta/l = 0.0625$. For all samples $t = 76.2 \mu\text{m}$ and $l = 12 \text{ mm}$. The kirigami sheet and the kirigami shell with $\delta/l = 0.0333$ pop up uniformly while the kirigami shell with $\delta/l = 0.0625$ exhibits a propagating pop-up deformation. Dashed squares shows the magnified regions.

Movie S4. Snapping propagation of pop-ups in a kirigami shell with triangular cuts.

Tensile response of a kirigami shell with triangular cuts characterized by 8×20 units with $\delta/l = 0.125$, $t = 76.2 \mu\text{m}$ and $l = 12 \text{ mm}$. This structure is characterized by a large energy barrier \mathcal{S}_1 , resulting in a sharp propagation front. As a result, the stress-strain curve of the structure is characterized by a discrete sequence of drops during propagation, each corresponding to the opening of one row of cuts. Dashed square shows the magnified region.

Movie S5. Kirigami with linear cuts: tensile response of sheet vs shell

Comparison between tensile deformation of three kirigami structures with linear cuts: (left) a flat kirigami sheet with 3×60 units, (middle) a kirigami shell with 4×60 units and (right) a kirigami shell with 20×60 units. For all samples $\delta/l = 0.2$, $t = 76.2 \mu\text{m}$ and $l = 12 \text{ mm}$. The kirigami sheet and the kirigami shell with $n = 4$ pop up uniformly, whereas the kirigami shell with $n = 20$ exhibits a propagative instability. Dashed squares shows the magnified regions.

Movie S6. Kirigami with orthogonal cuts: tensile response of sheet vs shell

Comparison between tensile deformation of three kirigami structures with orthogonal cuts: (left) a flat kirigami sheet with 2×20 units, (middle) a kirigami shell with 4×20 units and (right) a kirigami shell with 20×20 units. For all samples $\delta/l = 0.08$, $t = 76.2 \mu\text{m}$ and $l = 6 \text{ mm}$. The kirigami sheet and the kirigami shell with $n = 4$ pop up uniformly, whereas the kirigami shell with $n = 20$ exhibits a propagative instability. Dashed squares shows the magnified regions.

Movie S7. Finite element simulations

(1) Deformation of unit cells of three kirigami structures with triangular cuts up to $\bar{\epsilon} = 0.3$: (left) flat, (middle) initially curved, (right) rolled unit cells characterized by $n = 8$, $\delta/l = 0.0625$, $t = 76.2 \mu\text{m}$ and $l = 12 \text{ mm}$. The contours show the distribution of the *von Mises* stress.

(2) Comparison between deformation of two kirigami shells with triangular cuts characterized by $\delta/l = 0.0625$ and $\delta/l = 0.125$ with $n = 8$, $t = 76.2 \mu\text{m}$ and $l = 12 \text{ mm}$. For each case the response of the unit cell, super cell and visually tessellated super cell are shown. The contours show the distribution of the *von Mises* stress.

(3) Deformation of a kirigami shell with linear cuts characterized by $n = 20$, $\delta/l = 0.2$, $t = 76.2 \mu\text{m}$ and $l = 12 \text{ mm}$: (left) unit cell, (middle) super cell and (right) visually tessellated super cell. The contours show the distribution of the *von Mises* stress.

(4) Deformation of a kirigami shell with orthogonal cuts characterized by $n = 20$, $\delta/l = 0.08$, $t = 76.2 \mu\text{m}$ and $l = 20 \text{ mm}$: (left) unit cell, (middle) super cell and (right) visually tessellated super cell. The contours show the distribution of the *von Mises* stress.

Movie S8. Programming pop-ups

(1) Response of programmed kirigami sheet and kirigami shell under tension. These kirigami surfaces comprise an array of triangular cuts separated by ligaments with width $\delta/l = 0.125$ in the center and $\delta/l = 0.033$ near the two two ends.

(2) Performance of three crawlers skinned with kirigami shells which exhibit uniform, propagating and programmed pop-up.

Movie S9. Effect of imperfection

Deformation of an imperfect kirigami shells with triangular cuts which is characterized by $\delta/l = 0.125$ (with $l = 12 \text{ mm}$) and $n = 8$. An imperfection is introduced in the middle of the shell by decreasing the width of one row of hinges to $\delta/l = 0.0625$.

References

1. Abaqus, V., 2014. 6.14 Documentation. Dassault Systemes Simulia Corporation.
2. T.C. Shyu et al (2015). A kirigami approach to engineering elasticity in nanocomposites through patterned defects, *Nat Mat* 14:785–789.
3. A. Lamoureux, K. Lee, M. Shlian, S.R. Forrest, and M. Shtein (2015), Dynamic kirigami structures for integrated solar tracking, *Nat Commun* 6:8092.
4. M. Isobe and K. Okumura (2016), Initial rigid response and softening transition of highly stretchable kirigami sheet materials, *Sci Rep* 6:24758.
5. A. Rafsanjani and K. Bertoldi (2017), Buckling-induced Kirigami, *Phys Rev Lett* 118:084301.
6. A. Rafsanjani, Y. Zhang, B. Liu, S.M. Rubinstein and K. Bertoldi (2018), Kirigami skins make a simple soft actuator crawl, *Sci Robotics* 3(15):eaar7555.
7. M. Senn, C. Eberl, Digital Image Correlation and Tracking (2015). Available from: <https://uk.mathworks.com/matlabcentral/fileexchange/50994-digital-image-correlation-and-tracking>.
8. D. Polyzos, and D.I. Fotiadis (2012), Derivation of Mindlin’s first and second strain gradient elastic theory via simple lattice and continuum models, *Int J Solids Struct* 49:470-480.
9. R.D. Mindlin (1964), Micro-structure in linear elasticity, *Arch Ration Mech Anal* 16:51-78.
10. J.C. Maxwell (1875), On the dynamical evidence of the molecular constitution of bodies, *Nature* 11:357-359.
11. M. Danielsson, D.M. Parks, M.C. Boyce (2002), Three-dimensional micromechanical modeling of voided polymeric materials, *J Mech Phys Solids* 50:351-379.
12. A. Polyanin, V. Zaitsev, Handbook of nonlinear partial differential equations (Chapman and Hall/CRC, London, 2011).
13. T. Dauxois, M. Peyrard, Physics of solitons (Cambridge University Press, London, 2006).